Photoluminescence in MoS_2 Multilayers with Functional Polyelectrolyte Nanospacing

Kiyoung Jo

Department of Physics

Graduate School of UNIST

2015

Photoluminescence in MoS_2 Multilayers with Functional Polyelectrolyte Nanospacing

Kiyoung Jo

Department of Physics

Graduate School of UNIST

2015

Photoluminescence in MoS_2 Multilayers with Functional Polyelectrolyte Nanospacing

A thesis
submitted to the Graduate School of UNIST
in partial fulfillment of the
requirements for the degree of
Master of Science

Kiyoung Jo

01/ 06/ 2015

Approved by

Major Advisor
Byeong-Su Kim

Photoluminescence in MoS_2 Multilayers with Functional Polyelectrolyte Nanospacing

Kiyoung Jo

This certifies that the thesis of Kiyoung Jo is approved.

01/ 06/ 2015

signature

Thesis supervisor: [Byeong-Su Kim]

signature

[Kibog Park]

signature

[Kyung Rok Kim]

Contents

Abstract

Photoluminescence phenomenon in multilayers of molybdenum disulfide (MoS_2) spaced by nano-thick polyelectrolyte layers are demonstrated on behalf of various transition metal dichalcogenides. Using facile method of layer-by-layer (LbL) assembly, negative charged MoS_2 sheet and positive charged polymeric layers are sequentially stacked on various substrates. In this structure, individual MoS_2 monolayers are not only effectively screened from interlayer coupling but also p-doped by functional polymeric layers. The Raman analysis demonstrates that MoS_2 nanosheets separated by polymeric trilayers display much larger increase in photoluminescence (PL) as the number of layers is increased. Furthermore, it was also found that the enhanced PL has been correlated to the ratio of excitons to trions with type of polymeric spacers. Because uniform heterogeneous interfaces can be formed between various transition metal dichalcogenides and other soft materials, we expect that the result will be a trigger to fabricate hetero vertical architecture with other 2D analogues and will offer potential electronic and optoelectronic applications.

List of Figures

excitonic peaks corresponding to negatively charged trion (X^-) and neutral exciton (X^o). The binding energy of trion in $MoSe_2$ is 30 meV.

Figure 8. (a) PL plots of $MoSe_2$ as a function of gate voltage. Near the zero gate voltage, natural and impurity-trapped excitons exist. (b) Neutral exciton and charged trion peak intensity with the gate voltage.

Figure 9. PL spectrum of monolayer MoS_2 (a) before and after *p*-doping process with small molecules (TCNQ and F_4TCNQ) and (b) the PL spectrum before and after doping effect with an *n*-type dopant (NADH). (c) Illustration for charge transfer. Driving force is relative chemical potentials difference between monolayer MoS_2 and *n*- and *p*-type dopants.

Figure 10. (a) Optical photograph of an exfoliated MoS2 flake with indicated layer thicknesses of the different facets. (b) Quantum dot fluorescence lifetime map and (c) corresponding energy transfer efficiency map of the same flake.

Figure 11. (a) PL spectrum of monolayer MoS_2 that is immersed in anisole. Experimental data are fitted by three different Lorenztian functions. The inset demonstrate scheme of a trion and an exciton. (b) The PL peak positions versus the solvent dielectric constant. (c) The PL intensities normalized by the A_{1g} Raman vibrational mode intensities. (d) Raman shifts of the E^1_{2g} and A_{1g} vibrational modes as a function of the solvent dielectric constant. The inset schematics display the directions of the vibration. The plot indicates that there is negligible doping effect on MoS_2 after immersing to solvents.

Figure 12. (a) Stable dispersions of exfoliated 2D materials from solution-processable exfoliation method in solvents and films from vacuum filtration. (b) Stable MoS_2 monolayer solution in water fabricated by lithium-intercalated (left). Left picture shows images of MoS_2 from high-angle annular dark-field scanning transmission electron microscopy (HAADF-STEM) and right picture displays atomic force microscopy (AFM) image of flakes of MoS_2 on SiO_2. (c) Schematic representation of CVD growth of monolayer MoS_2 sheet from solid S and MoO_3 precursors and fabricated MoS_2 films. (d) Schematic representation of CVD growth of MoS_2. In this process, the growth was conducted by flowing vapor phase sulfur to the solid layer of Mo on SiO_2.

Figure 13. (a) Cross sectional scheme of a monolayer MoS_2 FET. 30 nm of Atomic layer deposition (ALD)-grown HfO_2 is deposited on the MoS_2 monolayer sheet. (b) Transfer characteristic curve at room temperature with 10 mV drain voltage V_{ds}. Inset transfer plot displays I_{ds}–V_{ds} curve with V_{bg} values of 0, 1 and 5 V.

Figure 14. (a) Photo-switching behavior of single-layer MoS_2 phototransistor with different light power (P_{light}) and drain voltage (V_{ds}). (b) Photo-switching rate and (c) consistency of photo-switching ability of monolayer MoS_2 phototransistor at V_{ds} = 1 V, P_{light} = 80 μW.

Figure 15. Electroluminescence (EL) intensity with monolayer MoS_2. EL is mainly observed near the metal contact because significant band bending of MoS_2 facilitates electron-hole recombination.

Figure 16. (a) Schematic representation of monolayer WSe_2 p-n junction. Two different gate-bias induces different carrier dominancy. (b) Electroluminescence from p-n junction with respect to drain current.

Figure 17. (a) Schematic representation of the LbL assembly and (b) MoS_2 multilayers nanospaced by single- and tri- layer, resepectively. (c) Digital photograph of MoS_2 multilayers film on quartz slide.

Figure 18. AFM image of MoS2 monolayer exfoliated by Li-intercalation and corresponding line scan profile.

Figure 19. Absorbance spectrum of (a) *n* M_{SL} and (b) *n* M_{TL} set. (*n* = the number of MoS_2 layers) Dotted line indicates excitonic peaks of each sample. Inset is schematic representation of MoS_2 multilayers nanospaced by polymeric single-layer and tri-layer.

Figure 20. (a) – (d) SEM images of 1 – 4 M_{TL}, respectively. The variation of contrast of each set exhibits level of layer is different. (e) Cross-section TEM image of $2M_{TL}$ and (f) corresponding line scan profile displaying the thickness of monolayer MoS_2 and polymeric tri-layer.

Figure 21. Ellipsometry measurement of *n* M_{TL} set.

Figure 22. (a) The Raman spectrum of vibrational modes of different layers of MoS_2 M_{TL} set and (b) its intensity. It indicates that film is gradually grown. (c) Peak position of each Raman vibrational modes. Blue dotted line exhibits peak difference of monolayer MoS_2. A_{1g} blue-shift results from p-doping process as indicated in red arrow. (d) Corresponding PL intensity of M_{TL} set. Inset is comparison of the PL intensity between M_{TL} and M_{SL} set. (e) The PL intensity of M_{TL} as a function of number of M_{TL}. Areal intensity is chosen to consider all electrons which are involved in luminescence. (f) Schematic representation of M_{TL} set. MoS_2 is described in yellow colored sulfur and grey colored Mo while polymeric chains are indicated by green (PAH/PSS/PAH) and blue color (PEI).

Figure 23. Comparison of PL intensity of (a) M_{SL} and (b) M_{TL} set as a function of wavelength dimension. All the intensities are normalized with Si 1st order peak at 520 cm^{-1}.

Figure 24. Devonvoluted High- resolution X-ray photoelectron spectroscopy (XPS) spectrum. (a) N 1s spectra of polymeric single layer (PAH) before and (b) after annealing. (c) XPS spectra of Mo 3d and (c) Sulfur 2p of 1 M_{TL} MoS_2 multilayer using previous result. Shirley background is applied to precise fitting.

Figure 25. Three-level system of excitonic states. Continuous optical generation (*G*) let the each excitonic quasi-particle (A^o and A^-) be in steady states. Γ_{A^o}, Γ_{A^-} and k_{A^-} are recombination rate of A^o, A^- and formation rate of A^-.

Figure 26. (a, b) Areal PL intensity of MoS_2 multilayers contributed from exciton and trion, respectively. Dotted lines are exponentially fitted line. (c, d) Deconvoluted PL spectrum of the M_{SL} and M_{TL} sets, respectively. (c, d) Ratios of trions and excitons for each layer and the corresponding electron density. (f) Photon energy of A band peaks in M_{TL} and M_{SL} sets.

Figure 27. Dimensionless interparticle distance in M_{SL} and M_{TL} set.

Figure 28. (a) Quantum yield of M_{TL} and M_{SL} sets. (b) full-width-at-half-maximum (fwhm) value of M_{TL} set.

Figure 29. (a) PL intensity mapping of M_{TL} set ($20 \times 20\ \mu m^2$) with a different number of MoS_2 layers. All mappings were conducted with 0.35 mW 532-nm laser for 0.1 s integration time. Signals are obtained from 1.7 to 2.1 eV for each data. (b) Nanospaced MoS_2 and WS_2 heterostructure fabricated by LbL assembly. Green and blue lines are peak difference between E^1_{2g} and A_{1g} of MoS_2 and WS_2, respectively.

Figure 30. Summary of photoluminescence phenomenon of MoS_2 multilayer.

I. Introduction

1.1 2-Dimensional Electronic System and Materials

1.1.1 2-Dimensional Electronic System and General Trends

Atomically thin 2-dimensional (2D) materials are defined as extremely thin, usually ~1 nm, material that *z*-directional confinement highly influences behavior of the electron.[1] 1st generation of 2D materials was graphene, which is monolayer of carbon honeycomb structure. It was anticipated that it exhibits remarkable electronic features which are not observed in common 3-dimensional materials. However, it had been expected that such 2D materials could not exist because they are thermodynamically unstable. Fortunately, it turned out that graphene can be successfully exfoliated into monolayer in 2004.[2] As a result, many researchers have made efforts to observe new physical phenomena and it becomes cornucopia of condensed matter physics and potential applications.[1,3] The marvelous physical features trigger the interests on various kinds of atomically thin 2-dimensional (2D) materials such as transition metal dichalcogenides, perovskites and black phosphorus to develop next-generation electronic devices.[4,5]

1.1.2 Graphene; Physical Features and Electronic Applications

Band structure of graphene, so called Dirac cone, reveals various physical features. Extraordinary feature is originated from the linearity between momentum and energy relation. Normally condensed matter physics describes charge carriers to the fermions with effective mass m^* according to Schrodinger equation which includes hyperbolic relation **(Figure 1a)**. However, the linearity reveals that charge carrier in graphene photon-like massless transport.[6] Therefore, massless transport in graphene should be described by Dirac equation rather than Schrodinger equation **(Figure 1b)**. Such a relativistic behavior provides facile way to proves researches on fundamental nature such as carrier transport, quantum hall effect.[7,8] Since speed of electron on the surface of graphene is $\frac{1}{300}c$ when c is speed of light, the electron mobility reaches extraordinary 100,000 cm^2/V^*s and therefore graphene is good candidate for future device applications.

Second, it can be easily inferred that graphene is semi-metal. At a glance, the conduction band and the valence band are attached at single point which is called Dirac point. At the Dirac point, the density of states is zero so that it seems there is no conductivity at this point. However, there is theoretical minimum conductivity of $\frac{4e^2}{\pi h}$ even when there is no charge carrier due to quantized conductivity **(Figure 2)**.[1] This semi-metal feature results in ambipolar behavior of transfer curve in FET, meaning that electron becomes carrier under positive gate voltage while hole is dominant under negative voltage **(Figure 3)**.[6] Such easy tunable carrier concentration brings about large interests on practical electronic devices. Since normal CMOS technology uses *n*- and *p*-MOSFET structure simultaneously, it is expected that graphene can effectively reduce chip size due to its ambipolar behavior.[1] However, semi-metallic properties limits its own applications since current electronic engineering is based on semiconductor. As a result, many researchers have tried to find and characterize 2-dimensional semiconductor.

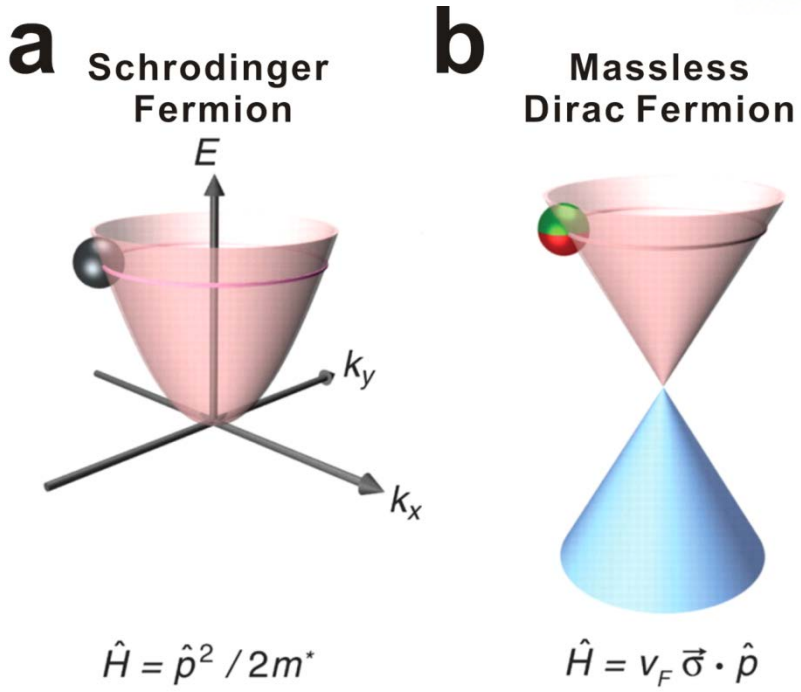

Figure 1. (a) Normal charge carrier model of Schrodinger equations in condensed matter physics. (b) Dirac cone structure of graphene. Linearity between momentum and energy displays massless transport of electron with Fermi velocity (v_F) of ~1 x 10^6 m/s.

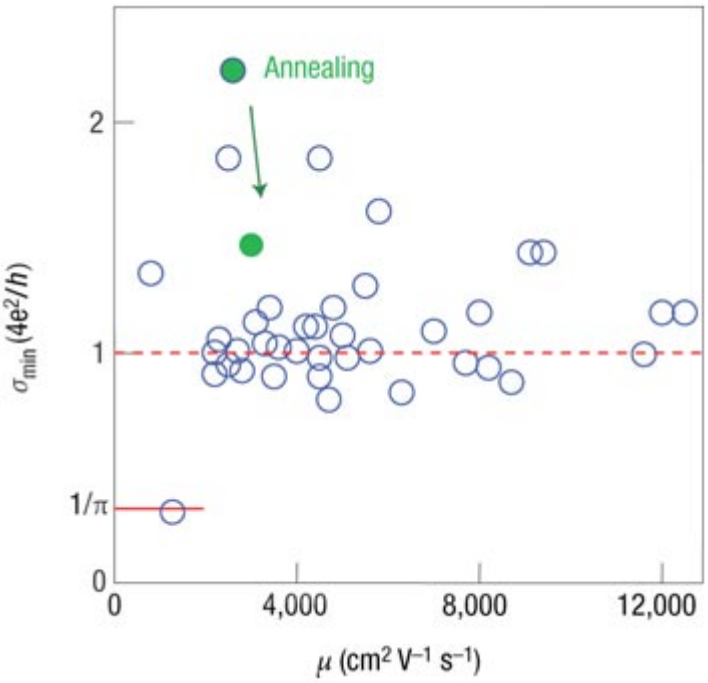

Figure 2. Minimum conductivity of graphene. The conductivity is largely independent to electron mobility. Theoretical conductivity of graphene is $\frac{4e^2}{\pi h}$ while most devices reach $\frac{4e^2}{h}$.

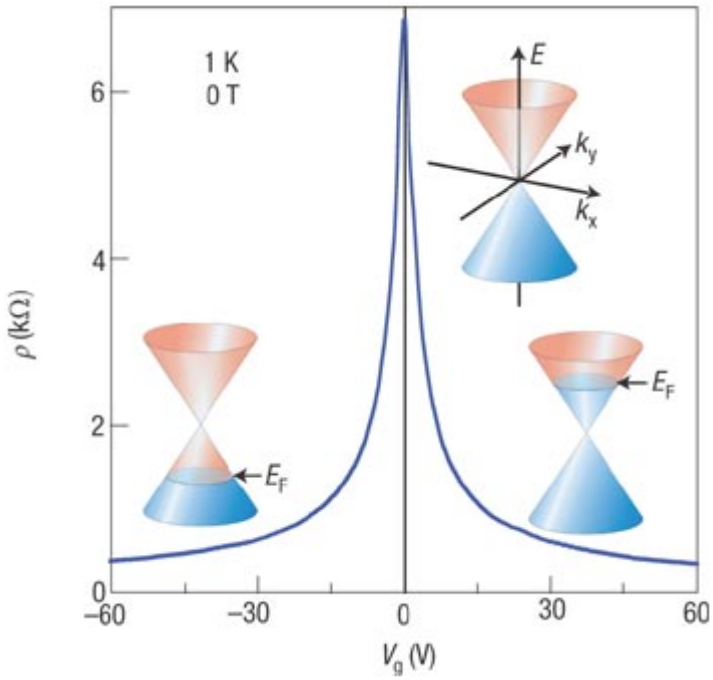

Figure 3. Ambipolar electric field effect on monolayer graphene. The inset plots indicate *E-K* diagram of graphene, the Dirac cone, with changes of the Fermi energy E_F. The rapid decrease in resistivity along the gate voltage shows high mobility, ~100,000 $cm^2/V*s$.

1.1.3 Transition Metal Dichalcogenides

Since the discovery of graphene, marvelous features of 2D electron system triggers fundamental characterization of other layered materials.[9] Transition metal dichalcogenides (TMDs) are promising platform of the 2D materials which are composed of transition metal sandwiched by outer sheets of chalcogen atoms. 2D TMDs have various kinds of combinations with transition metal elements of group 4 to 10 and several chalcogen atoms with the stoichiometry of MX_2, where M is transition metal and X is chalcogen atom **(Figure 4a)**.[10,11] The large family of TMDs appear diverse electronic properties with their own elemental combinations. For example, group 6 metal elements with chalcogen atom displays semiconducting behavior. While HfS_2 acts as insulator. Moreover, some of the TMDs with group 5 elements show metallic or even superconducting.[10]

There are two kinds of structure of the monolayer of TMDs; trigonal prismatic and octahedral coordination. The stacking order is varied by the two kinds of coordination environments. With trigonal prismatic structure, it forms AbA stacking with the formation which is very similar to honeycomb structure of graphene from *z*-directional point of view while octahedral coordination reveals AbC stacking **(Figure 4b, c)**.[11] In Nature, they formed stable layered structure bonded by van der Waals force. Since van der Waals force is weak enough to peel off, monolayer can be exfoliated.

The thickness of the monolayer reaches 6~7 Å, which is fairly enough to build *z*-directional quantum confinement effects. The confinement effects perturb the band structure which opens up new phenomenological and technological developments. These several factors such as composition, phase engineering and thickness influence the electronic properties of TMDs.

The general tendency of band structure with various TMDs is described in **Figure 5a**.[11] The location of the Fermi level of each set represents electronic properties. Band structure of TMDs is mainly determined by *d*-orbitals of transition metal and chalcogen atom. Firstly, octahedral structured transition metal centres (D_{3d}) of TMDs form degenerated band structure composed of $d_{z^2,\,x^2-y^2}$ and $d_{xy,yz,zx}$ orbitals while trigonal prismatic coordination (D_{3h}) gives rise to the band structure consisting of d_{z^2}, $d_{x^2-y^2,xy}$ and $d_{xz,yz}$ orbitals. Since gap between these orbitals in trigonal prismatic coordination is ~1 eV, the TMDs with the adequate Fermi level can be good candidates for semiconductor.

The electronic band structure of monolayer TMDs is changed due to elimination of interlayer coupling and quantum confinement effects. Especially, 2D semiconductor reveals significant changes in band structure. Monolayer 2D TMD semiconductor becomes direct semiconductor while its bulk counterpart displays indirect semiconducting behavior. Bulk semiconductor TMDs show ~1 eV of bandgap with transition from valence band maximum at Γ point to conduction band minimum at midpoint along $\Gamma - K$ **(Figure 5b)**.[11-13] In the monolayer limit, however, direct bandgap appears at K

point which is located at 6 corners of first Brillouin zone **(Figure 5b, c)**.[14,15] The reason for indirect-to-direct transition is explained by effective mass.[12] The out-of-plane mass of electron and hole near the K point is much larger than free electron mass m_o. However, out-of-plane mass for holes near the Γ point is ~$0.4m_o$ and for electrons near the midpoint along $\Gamma - K$ is ~$0.6m_o$. As the number of layers decreases, effective masses related to indirect transition are drastically increased while effective masses at K point are largely unchanged. As a result, in the monolayer limit, indirect bandgap becomes larger than direct bandgap and therefore 2D TMD semiconductor reveals direct band structure. The transition becomes the basis of significant increase in PL by ~10^3 times compared to the bulk.[12] Furthermore, there are two characteristic peaks are observed by valence band splitting by large spin-orbit coupling of ~180 meV at the K point.[16] Therefore, two kinds of peaks, which are assigned as A and B, are observed in PL spectrum.[17,18]

The family of TMDs are very promising materials due to the exotic properties as described above. These features trigger the researches regarding on fundamental physics such as valley hall effect[19], many-body physics[20] and potential applications in optoelectronics and high-performance field-effect transistors.[20-22]

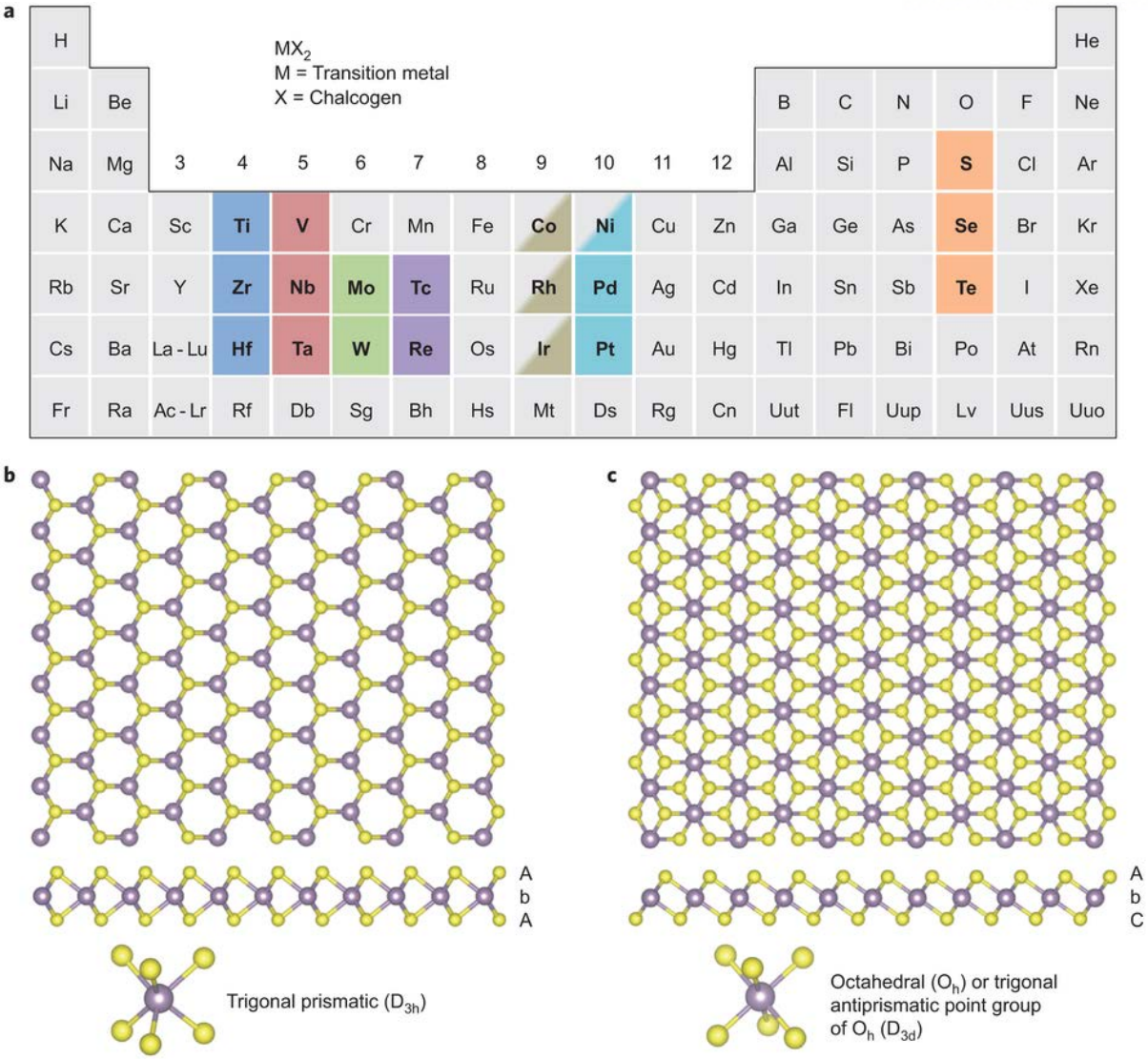

Figure 4. (a) Periodic table which highlights the composition of TMD sets. ~40 different layered compounds exist. (b) Point of view along c-axis with trigonal prismatic (c) and octahedral arrangement. Transition metal is colored with purple while chalcogen atoms are colored with yellow. The stacking orders are indicated with labels AbA and AbC, respectively.

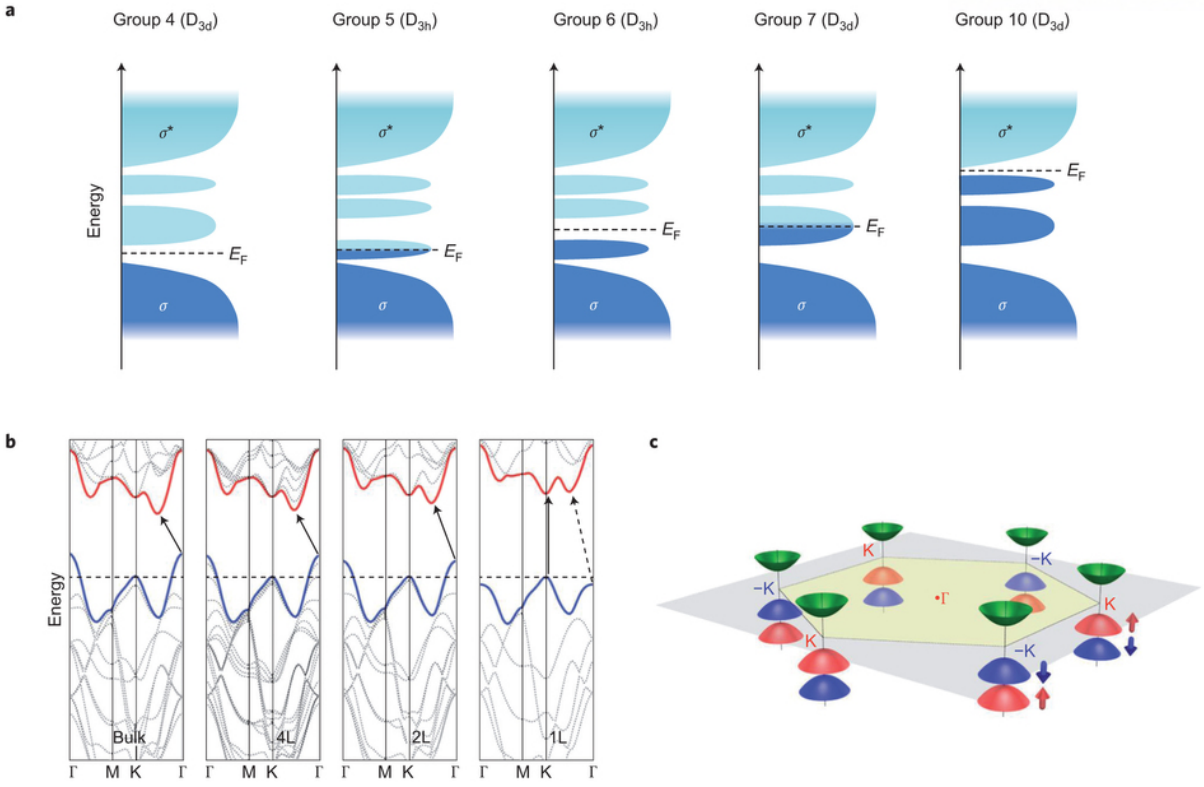

Figure 5. Schematic illustration of general band structure within the group 4 - 10 TMDs. D_{3h} and D_{3d} denote to the point group related to the trigonal prismatic and the octahedral coordination (b) Energy-momentum diagram of MoS_2 in bulk to monolayer. The red and blue solid lines indicate the conduction minimum and valence maximum, respectively. The solid arrows indicate the lowest energy transition which displays that only monolayer is direct semiconductor. (c) First Brillouin zone of MoS_2 showing six valleys and valence band splitting by spin–orbit coupling at the K points. The green surfaces illustrate the conduction band and its minimum. The red and blue surfaces exhibit split valence band maxima.

1.2 Excitonics and Photoluminescence

1.2.1 Excitons and Photoluminescence in 2-Dimensional Electronic System

When photon is injected to the surface, optical transition in semiconductor or insulator should take the electron-hole Coulomb interaction into account by solving Schrodinger equation with approximated hydrogen atom.[23] It naturally produces the bound quasi-particle composed of electron and hole, namely exciton. The quasi-particle significantly alters the shape of band edge. As a result, electronic bandgap becomes different to the optical bandgap. Optical bandgap is related as electronic bandgap minus binding energy of the exciton. In that way, exciton acts important role in luminescence behavior in semiconductor.

2D character of monolayer TMD is highly confined electron system in *z*-direction. The reduced dimensionality dominates the optical and charge-transport features.[24] One critical factor is strong enhancement of the Coulomb interaction. Furthermore, the highly confined system provides rapid change of dielectric environment **(Figure 6a)**.[25] The exciton on the 2D semiconductor experiences reduced dielectric screening, which lets electric field from exciton extends outside of the sheet. These effects bring about two important features. Firstly, bandgap is increased by confinement effect **(Figure 6b)**. Second, the strong Coulomb interaction results in increase of binding energy of exciton. Additionally, reduced dielectric screening also contributes to strengthen the binding energy. For example, binding energy in 2D materials records 0.5 ~ 1 eV which is an order of magnitude larger than previously reported quasi 2D quantum well structures.[16,20,26-28]

Another interesting feature of 2D electron system is the stability of trion.[20] Trion is charged exciton which is formed by binding of additional charge carrier to neutral exciton. The trion binding energy in monolayer TMDs is 10 times larger than that of conventional quasi-2D system. For example, the binding energy in TMDs reaches 20-30 meV while semiconductor quantum well structure such as CdTe-Cd_{1-x}ZnTe (~2.65 meV) and GaAs (~1.2 meV) exhibits lower values **(Figure 7)**.[29,30] Furthermore, the trion is even observable in room temperature since thermal energy at room temperature is K_BT = ~26 meV.

Due to the remarkable characters of 2D system, huge amount of researches on practical optoelectronic applications of 2D materials have been conducted. For practical usage, many researchers have tried to improve photoluminescence by placing dielectric substrate or hBN, applying strain, fabricating large-grained MoS_2, gate biasing, covering by oxide, defect engineering and chemical doping controls.[22,31-39]

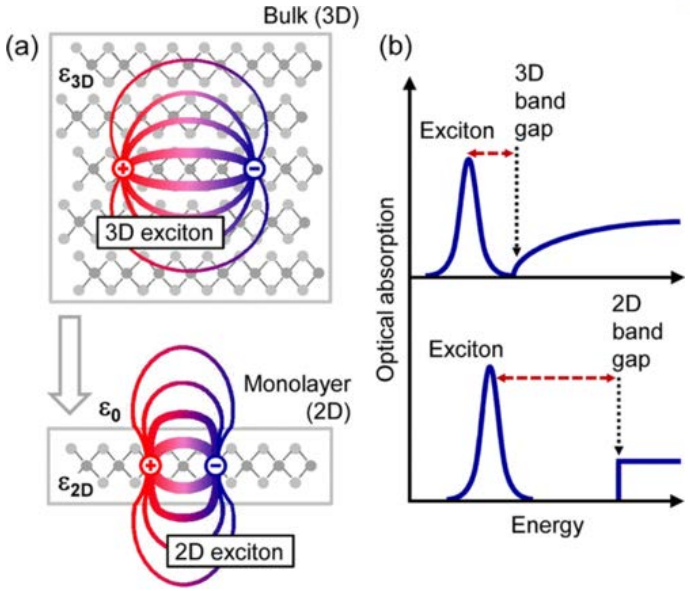

Figure 6. (a) Real-space representation of exciton in the 3D and 2D system. To demonstrate changes of dielectric environment, different dielectric constants ε_{3D} and ε_{2D} and by the vacuum permittivity ε_0 are shown. (b) Optical absorption with the dimensionality. The dashed red line indicates exciton binding energy. The transition from 3D to 2D is expected to lead to an increase of both the band gap and the binding energy.

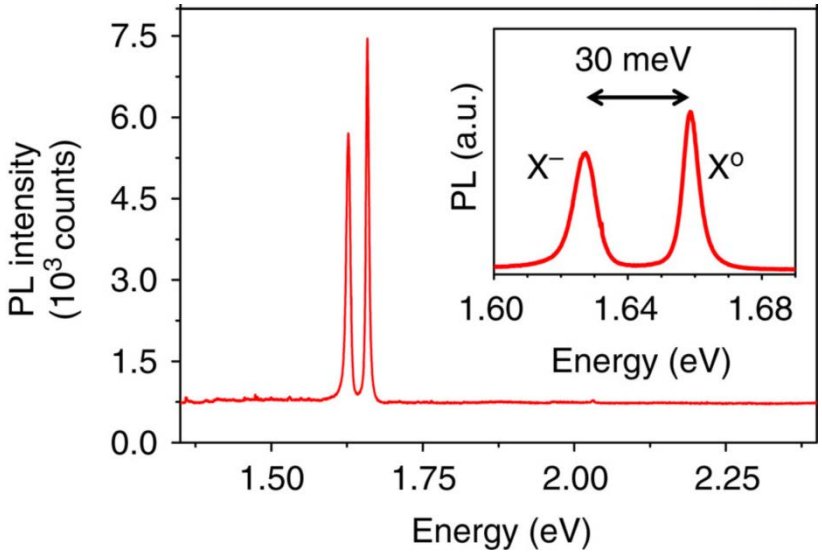

Figure 7. PL spectrum of $MoSe_2$ when electrons are excited with 2.33 eV laser. It shows two distinct excitonic peaks corresponding to negatively charged trion (X^-) and neutral exciton (X^o). The binding energy of trion in $MoSe_2$ is 30 meV.

1.2.2 Doping Effect and Photoluminescence

The interplay between neutral exciton and charge infers that exciton density can be manipulated by charge density control. Previous reports demonstrate electrical and chemical control can successfully enhance the PL intensity. In first, electrical control of carrier density can be conducted by gate-bias. **Figure 8a** exhibits gate voltage (V_g) dependent excitonic contribution on PL intensity with photon energy.[16] When V_g is zero, there exist two excitons, neutral exciton and exciton by impurities. **Figure 8b** displays easily displays the density of charged and neutral excitons deviated by V_g shifts. For example, sheet is *p*-doped and free hole becomes dominant with negative V_g. Corresponding PL is originated from positively charged trion. On the other hand, electron is dominant in positive V_g region and therefore negative trion mainly contributes to PL.

There were lots of chemical approaches to dope the monolayer MoS_2 which is the representative of TMD semiconductor. By using small molecule[38,40-42], gaseous phase molecule[39,43], self-assembled silane group, atoms[44,45] and nanoparticles[46] and various dielectric substrates[32], PL spectrums were varied according to the type of doping carrier and transfer rate. The common thing among the phenomenon is that *p*-type dopant increases PL while *n*-type dopant decreases it. For example, doping effect was investigated with small molecules such as *p*-type molecules (2,3,5,6-tetrafluoro-7,7,8,8-tetracyanoquinodimethane; F_4TCNQ, 7,7,8,8-tetracyanoquinodimethane; TCNQ) and *n*-type molecule, (nicotinamide adenine dinucleotide; NADH).[38] Through the simple drop-casting method, it revealed successful doping toward MoS_2. The PL intensity was drastically increased with *p*-dopant **(Figure 9a)** while *n*-dopant degrades it **(Figure 9b)**. The reason for this phenomenon is that MoS_2 is unintentionally *n*-doped and therefore the number of neutral exciton is increased by *p*-doping process. Furthermore, it was elucidated that chemical potential difference between MoS_2 and dopant is also important **(Figure 9c)**.

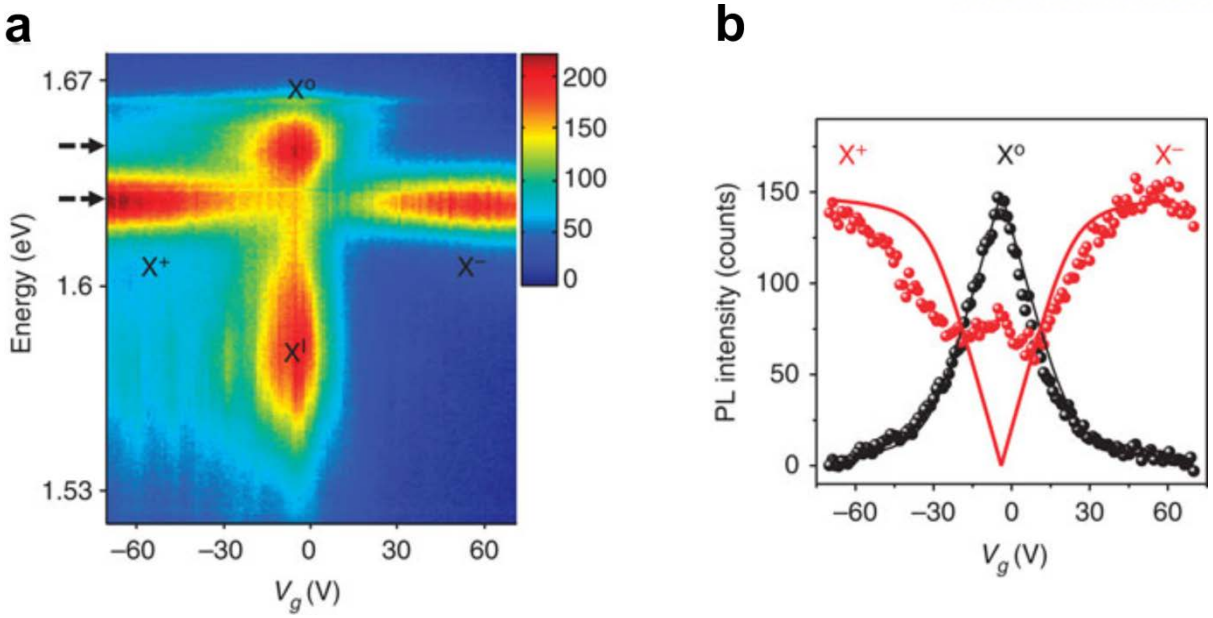

Figure 8. (a) PL plots of $MoSe_2$ as a function of gate voltage. Near the zero gate voltage, natural and impurity-trapped excitons exist. (b) Neutral exciton and charged trion peak intensity with the gate voltage.

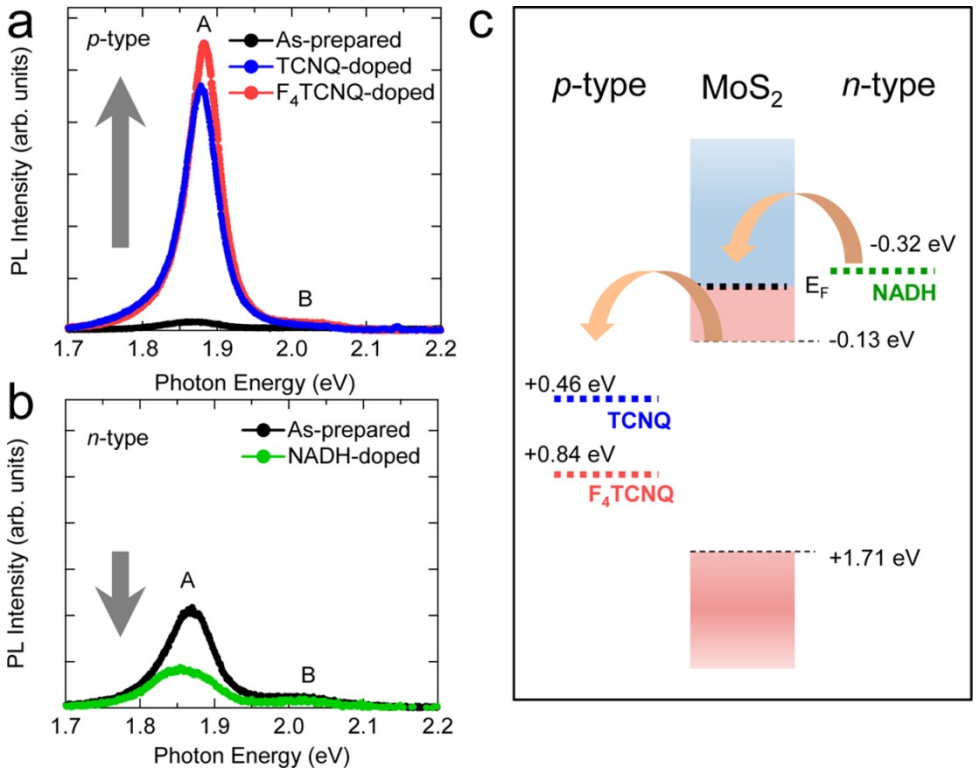

Figure 9. PL spectrum of monolayer MoS_2 (a) before and after *p*-doping process with small molecules (TCNQ and F_4TCNQ) and (b) the PL spectrum before and after doping effect with an *n*-type dopant (NADH). (c) Illustration for charge transfer. Driving force is relative chemical potentials difference between monolayer MoS_2 and *n*- and *p*-type dopants.

1.2.3 Dielectric Environment on Photoluminescence

Reduced dielectric screening plays significant role in 2D electron system due to prompt change of dielectric environment. Some researchers use this feature to observe meaningful phenomenon and extract practical usages. Recently, PL phenomenon in quantum dot/MoS_2 hybrid structure was observed to investigate energy transfer.[47] It turned out that PL intensity of quantum dot is efficiently quenched as the number of MoS_2 layers becomes thinner **(Figure 10a, b)**. It means energy transfer from quantum dot to MoS_2 is maximized in monolayer **(Figure 10c)**.

PL intensity variation as a function of dielectric environment was also analyzed with neutral exciton and negative trion because surrounding dielectric significantly influence the binding energy of excitons on the 2D materials **(Figure 11a)**.[48] Some researches were conducted with changing dielectric environment. Variation of dielectric environment induced change in binding energy of exciton and corresponding photoluminescence peak position and intensity. As MoS_2 was immersed in high-*k* solvent, PL peak intensity was increased because binding energy was diminished **(Figure 11 b,c)**. For accurate analysis, non-ionic dielectrics were used to minimize doping or adsorption effect from ionic particles **(Figure 11 d)**.

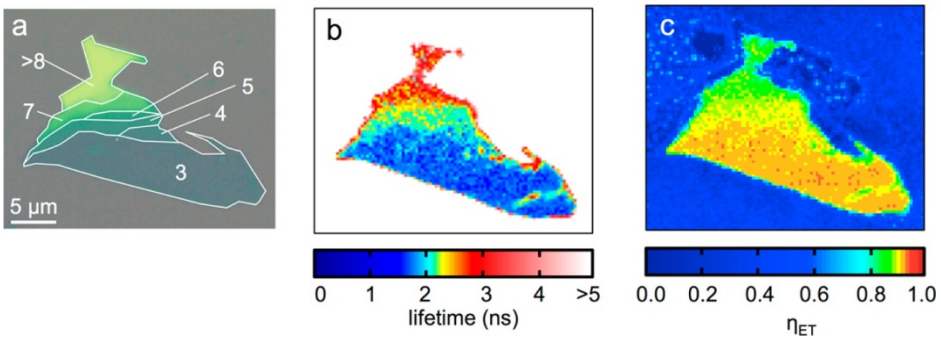

Figure 10. (a) Optical photograph of an exfoliated MoS2 flake with indicated layer thicknesses of the different facets. (b) Quantum dot fluorescence lifetime map and (c) corresponding energy transfer efficiency map of the same flake.

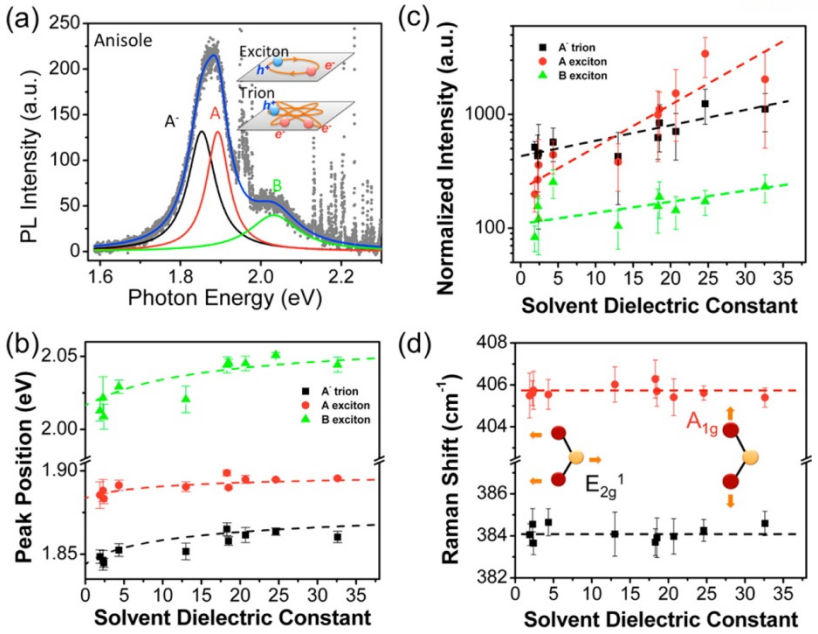

Figure 11. (a) PL spectrum of monolayer MoS_2 that is immersed in anisole. Experimental data are fitted by three different Lorenztian functions. The inset demonstrate scheme of a trion and an exciton. (b) The PL peak positions versus the solvent dielectric constant. (c) The PL intensities normalized by the A_{1g} Raman vibrational mode intensities. (d) Raman shifts of the E^1_{2g} and A_{1g} vibrational modes as a function of the solvent dielectric constant. The inset schematics display the directions of the vibration. The plot indicates that there is negligible doping effect on MoS_2 after immersing to solvents.

1.3 Fabrication of TMDs and Practical Application

1.3.1 Methods for synthesizing TMD layer

Reliable synthesis of TMD is very important for practical electronic applications since electronic or optoelectronic applications need uniform interfaces to minimize scattering and facilitate carrier transport. There are several methods for fabricating uniform 2D TMD sheets. Top-down and bottom-up methods have their own merits and disadvantages.

Firstly developed top-down method is mechanical cleavage method.[2,4] The method uses adhesive tape and the monolayer is transferred to substrate after careful finding of it. This method is very useful in purpose for phenomenological researches because it produces highly purified single-crystal flakes that are suitable for fundamental characterization. However, since it is extremely hard to find the monolayer sheet in reproducible manner, the alternative is necessary for practical applications.

To synthesize large quantity of monolayer sheets, solution-process based exfoliation is actively investigated **(Figure 12a, b)**.[49,50] The basic process is intercalation of ionic species into layered structure. Organolithium such as *n*-butyllithium is used because Li is smallest solid particles **(Figure 12b)**.[50] After successful intercalation within several days, the sample is immersed into water to generate vigorous evolution of gaseous phase H_2. Due to rapid extension of volume is driving force of chemical exfoliation. Such chemical exfoliation produces sub-micro scale sized sheets with large quantity. However, solution can dope or adsorb into surface and therefore it severely degrades electronic properties of 2D TMDs by generating defect or scattering center.

To fabricate high purity and large scale TMDs, chemical vapor deposition (CVD) process has been developed **(Figure 12c, d)**.[51-53] The representative method of CVD growth is evaporation and re-deposition process of sulfur powder and MoO_3 precursor by high temperature heating. These methods provide decent quality of wafer-scale sheets but it is still hard to fabricate monolayer thickness.

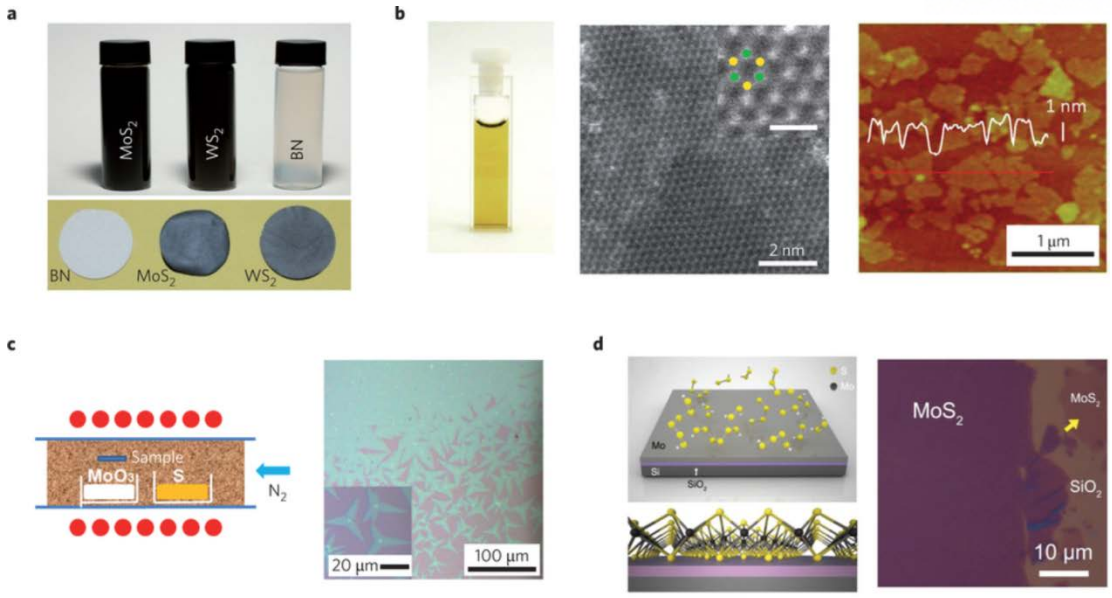

Figure 12. (a) Stable dispersions of exfoliated 2D materials from solution-processable exfoliation method in solvents and films from vacuum filtration. (b) Stable MoS_2 monolayer solution in water fabricated by lithium-intercalated (left). Left picture shows images of MoS_2 from high-angle annular dark-field scanning transmission electron microscopy (HAADF-STEM) and right picture displays atomic force microscopy (AFM) image of flakes of MoS_2 on SiO_2. (c) Schematic representation of CVD growth of monolayer MoS_2 sheet from solid S and MoO_3 precursors and fabricated MoS_2 films. (d) Schematic representation of CVD growth of MoS_2. In this process, the growth was conducted by flowing vapor phase sulfur to the solid layer of Mo on SiO_2.

1.3.2 Nanostructures for Optoelectronic Applications

Based on that knowledge, many approaches have been developed for potential application on optoelectronic devices. As a basic approach, firstly, field-effect transistor (FET) with HfO_2 dielectric was fabricated **(Figure 13a)**.[54] Because of successful suppression of the Coulomb scattering by HfO_2, the FET reached electron mobility of 217 $cm^2/V*s$ with current on/off ratio exceeding 1 x 10^8. It also reaches subthreshold swing value of ~74 mV/dec, which reflects efficient working efficiency **(Figure 13b)**.

To use remarkable photo-responsivity of MoS_2, phenomenological approaches were conducted with FET form.[55,56] When light is injected to common back-gated monolayer MoS_2 FET, photo-excited carriers in MoS_2 open electron channel as a response to the light **(Figure 14a)**.[57,58] Since it is very thin, charge density is easily tuned and therefore it reached prompt photo-switching rate of 50 ms **(Figure 14b)** with high stability **(Figure 14c)**.[57] Such direct semiconductor with fast responsivity will be good candidate for high-speed photodetector. For this purpose, several studies on hetero-vertical structures were also investigated. Since MoS_2 is able to absorb light and provide photoelectron while graphene exhibit massless transport, fast-responsive phototransistor can be fabricated. Actually, several researchers observed strong photocurrent in junction of graphene and MoS_2.[59,60]

In terms of luminescence behavior, electroluminescence (EL) behavior was further observed by simple applying voltage bias.[56] Injected electrons from electrode recombine with the holes in the sheet. Interestingly, EL was observed near the highly biased electrode because conduction band near the contact experiences strong band bending **(Figure 15)**. Therefore, injected electron contributes to the generation of excitons via impact excitation.

Furthermore, using the gate dependent charge density variation of 2D materials, 2 parallel gates were prepared to observe diode behavior in the monolayer **(Figure 16a)**.[61-63] In this structure, hole is dominant with negative gate voltage while electron dominant with positive voltage. As a result, p-n junction is formed in the monolayer and electron-hole recombination generated light **(Figure 16b)**.[63]

However, natural limitation of 2D material for device application is spatial ineffectiveness. The reason for this is that vertical stacking degrades exotic 2D characters. For this reason, studies regarding on multilayered structure have not been investigated. However, it is important to study on multilayered structure maintaining 2D characters for future applications.

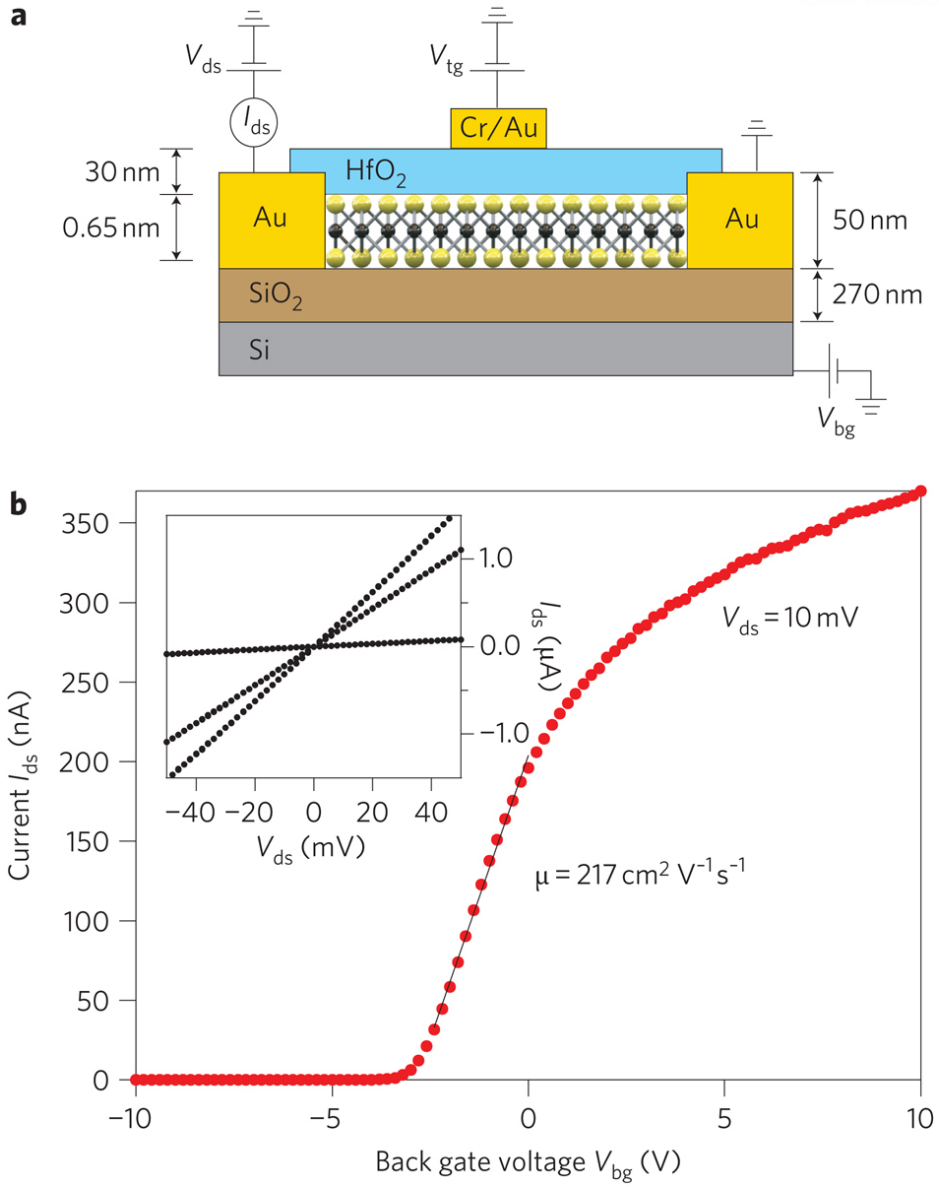

Figure 13. (a) Cross sectional scheme of a monolayer MoS_2 FET. 30 nm of Atomic layer deposition (ALD)-grown HfO_2 is deposited on the MoS_2 monolayer sheet. (b) Transfer characteristic curve at room temperature with 10 mV drain voltage V_{ds}. Inset transfer plot displays I_{ds}–V_{ds} curve with V_{bg} values of 0, 1 and 5 V.

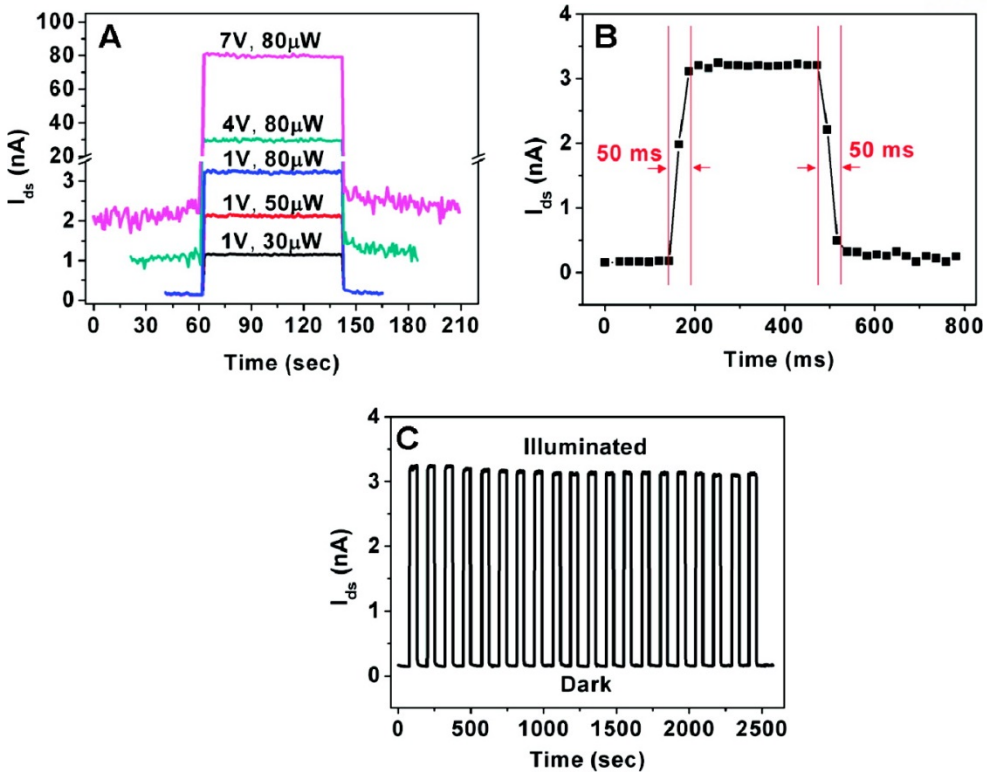

Figure 14. (a) Photo-switching behavior of monolayer MoS_2 phototransistor with different light power (P_{light}) and drain voltage (V_{ds}). (b) Photo-switching rate and (c) consistency of photo-switching ability of monolayer MoS_2 phototransistor at V_{ds} = 1 V, P_{light} = 80 μW.

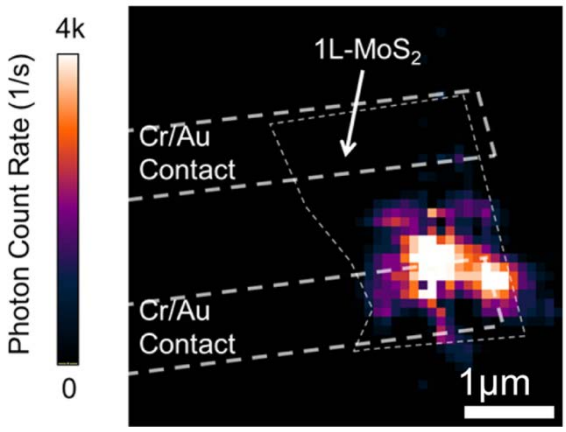

Figure 15. Electroluminescence (EL) intensity with monolayer MoS_2. EL is mainly observed near the metal contact because significant band bending of MoS_2 facilitates electron-hole recombination.

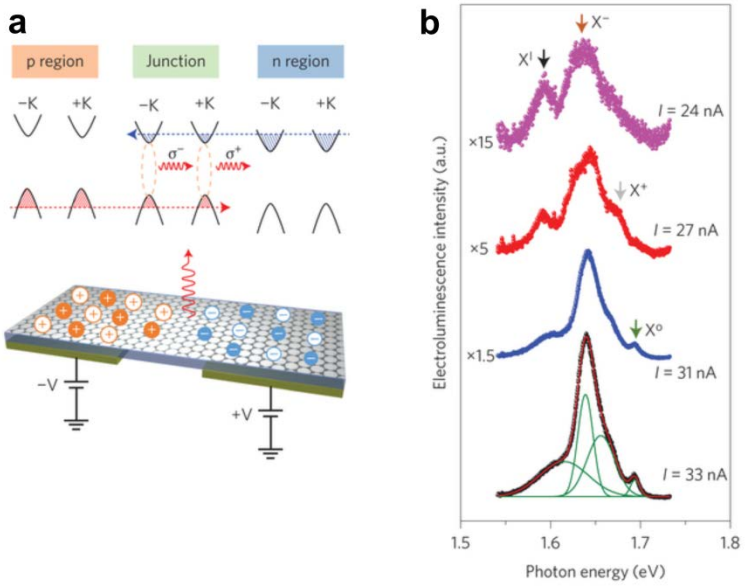

Figure 16. (a) Schematic representation of monolayer WSe_2 p-n junction. Two different gate-bias induces different carrier dominancy. (b) Electroluminescence from p-n junction with respect to drain current.

II. Experimental

2.1 Materials

2.1.1 Synthesis of MoS_2 Colloidal Suspension

MoS_2 colloidal suspension was prepared by Li-intercalation as described in previous reports.[17,50] In brief, MoS_2 powder (Sigma-Aldrich) was mixed with *n*-butyllithium in hexane (anhydrous 99%, Aldrich) and heated for 2 days at 95 ^oC under Ar ambient condition. After the drying process, the Li-intercalated MoS_2 powder was immersed in DI water. Then Li atom oxidized and evolved gaseous phase H_2 which resulted in successful exfoliation of MoS_2 monolayers. In that process, negatively hydroxide group were adsorbed on the surface defects in MoS_2 and therefore negatively charged stable suspension were formed. Purification was conducted by several centrifuges to eliminate Li ions.

2.1.2 Layer-by-Layer (LbL) Assembly

Figure 17a displays Layer-by-Layer assembly, which explains that both negatively charged MoS_2 suspension and positively charged polymeric suspension were sequentially stacked by electrostatic interaction between colloids. Polymeric layers were composed of poly (allylamine hydrochloride) (PAH) and poly (styrene sulfonate) (PSS). All the solutions were set into pH 7 to minimize adsorption of foreign ions. Negative charges were induced to substrate by piranha and O_2 plasma treatments. After that, poly (ethylene imine) (PEI) was deposited to uniform the layer and induce the positive charges. As polymeric spacer, two kinds of polymeric layers are formed to investigate interlayer coupling behavior. The thinner layer was PAH (single layer; SL) and the thicker one was PAH/PSS/PAH (trilayer; TL). Single layer step was conducted with 10 minutes dipping and 3 minute rinsing. All the samples were annealed at 300 ^oC to restore semiconducting behavior of MoS_2.[17] The resultants were therefore SiO_2/PEI/$(MoS_2/PAH)_{n-1}$/MoS_2 (*n* = number of single layers, *n* = 1-4) for multilayers nanospaced by single-layer and SiO_2/PEI/$(MoS_2/PAH/PSS/PAH)_{m-1}$/$MoS_2$ (*m* = number of tetralayers, *m* = 1-4) and by tri-layer (**Figure 17b)**. Hereafter both multilayers are denoted to *n* M_{SL} (multilayers spaced by polymeric single-layer) and *n* M_{TL} (multilayers spaced by polymeric tri-layer).

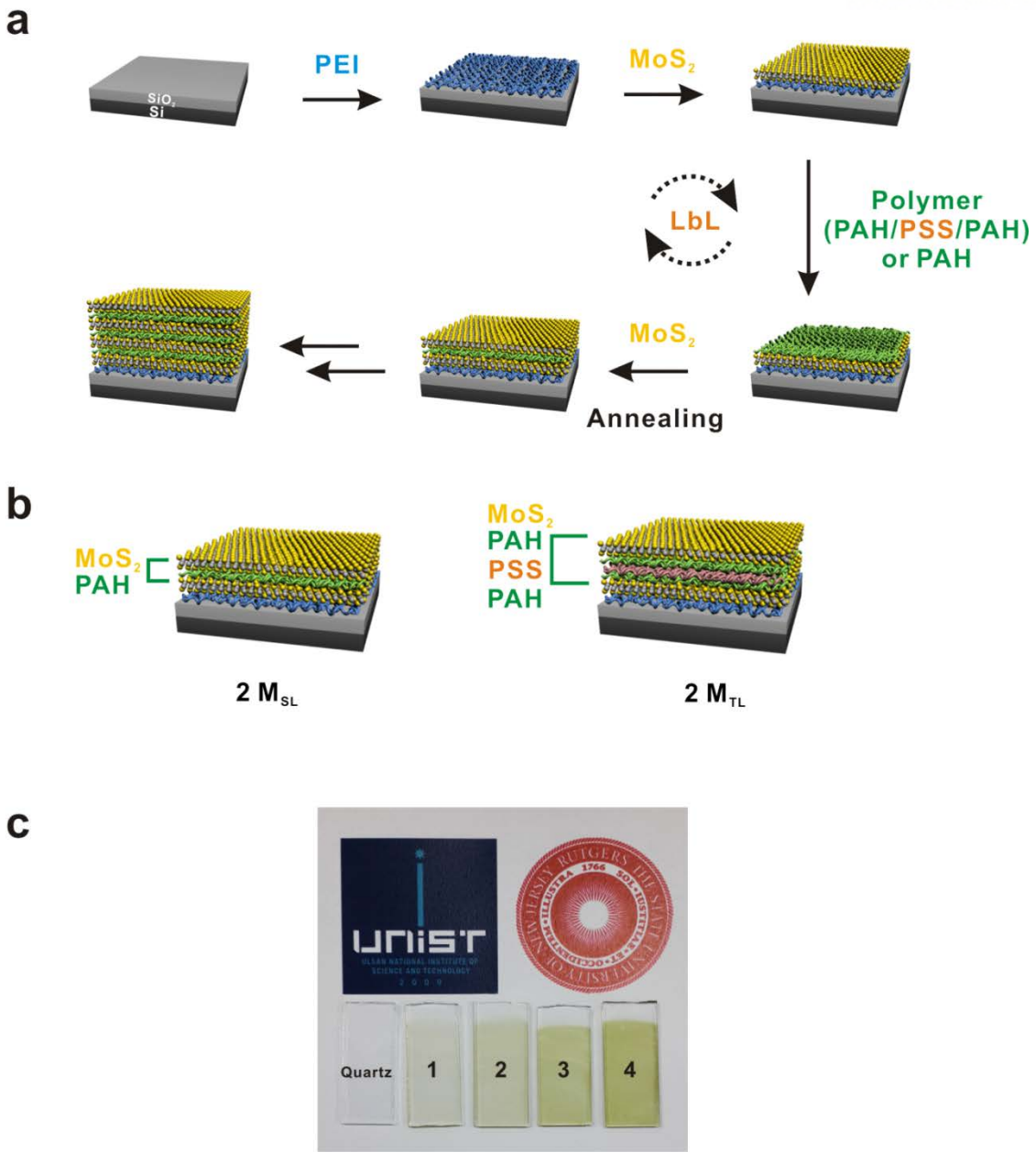

Figure 17. (a) Schematic representation of the LbL assembly and (b) MoS_2 multilayers nanospaced by single- and tri- layer, resepectively. (c) Digital photograph of MoS_2 multilayers film on quartz slide.

2.2 Measurement and Characterization

2.2.1 The Raman Spectrum

The Raman spectrum was measured by hand-made Raman instrument to observe the Raman vibrational modes and PL of both M_{SL} and M_{TL} sets.[64] As the excitation source, 514.5 nm Ar ion laser with 0.35 mW was used. The spectral resolution which is linewidth of the Rayleigh peaks was 6 cm^{-1} and 13 cm^{-1} for the Raman vibrational mode and PL. In this study, spectrum for each set was measured from 5 different points with the same focal spot. In addition, all the PL spectra are normalized with 1st order peak of a silicon substrate according to the.[13] Moreover, to avoid distortion of Raman signal due to thickness of SiO_2, PL of MoS_2 multilayers were also measured on both 285-nm and 300-nm-thick SiO_2 substrates and both results showed the same tendency.[65] Through these processes, the enhancement of PL is meaningful enough and it does not lose generality. For the Raman mapping, 532 nm laser with 0.35 mW was used. 40 Points were measured in each 20 μm lateral line with 0.1s signal integration. Filtering range was 2400 – 5100 cm^{-1}, which were corresponding to 1.7 – 2.1 eV in energy dimension.

2.2.2 Absorbance Spectrum and Quantum Yield

Absorbance of the films was characterized using a UV-vis spectrometer (VARIAN, Cary 5000). For PL quantum yield (QY) measurement, MoS_2 multilayers were prepared on quartz substrates. The data were collected by spectrofluorometer equipped with an integrating sphere (FP-8500, Jasco). All the values were corrected by indirect excitation of each sample referenced to rhodamine 6G.[12]

2.2.3 Structure Assessment

MoS_2 thickness was verified by tapping-mode atomic force microscopy (AFM) (Nanoscope IV, Veeco). To investigate film morphology, scanning electron microscopy (SEM) was used (Cold FE-SEM, Hitachi). High-resolution cross-sectional transmission electron microscopy (TEM) images were observed with a probe forming (STEM) Cs corrector at 200 kV (JEOL JEM 2100F system). Cross-section sample is prepared by Focused Ion Beam (Helios 450HP-Dual-Beam Focused Ion Beam) equipped SEM. Film thickness was measured by ellipsometry (EC-400 and M-2000 V, J. A. Woollam Co., Inc.). The thickness was measured 5 times for each sample and averaged value is used.

III. Results and Discussion

3.1 Inner Structure Observation

3.1.1 MoS_2 Exfoliation

To investigate how MoS_2 was successfully exfoliated, thickness was measured by tapping mode of Atomic force microscopy (AFM). The thickness of chemically exfoliated MoS_2 monolayer was ~ 1 nm according to the AFM image **(Figure 18)**. Although the value is a little higher than that of exfoliated sheet by common scotch-tape exfoliation method, it is originated from the presence of surface wrinkle or adsorbed or molecules.[17] Therefore it was concluded that the MoS_2 used in this study was successfully exfoliated into monolayer.

3.1.2 Absorbance Spectrum

Through the absorbance spectrum, a variety of information such as the film thickness and electrical transition can be observed. Firstly, the absorbance data of 1-4 multilayers are compared by UV absorbance spectrum to demonstrate successful growth of the film. The spectrum indicates gradual increase in the spectrum for each set **(Figure 19a, b)**. Although different kinds of polymeric layers were used for M_{SL} and M_{TL} set, the values were similar to each other.

Furthermore, excitonic peaks were investigated to confirm the optical band structure. MoS_2 has two characteristic excitonic peaks, named A and B peaks, due to spin-orbit coupling at K point in first Brillouin zone. Previous report states that both excitonic peaks display red-shift in peak position due to interlayer coupling between individual MoS_2 sheets.[17] The coupling induces direct to indirect bandgap transition and corresponding optical degradation. Therefore screening interlayer coupling in multilayered MoS_2 structure is essential for practical applications. For this purpose, polyelectrolyte spacer is introduced between MoS_2 monolayers. To assess screening of interlayer coupling along the thickness, two different thicknesses of polymeric spacers, that is, SL and TL were introduced between individual MoS_2 sheets. The M_{SL} set displayed slight red-shift in both excitonic peaks meaning that there was interlayer coupling despite of separation between MoS_2 sheets **(Figure 19a)**. On the other hand, A and B excitonic peaks in M_{TL} set revealed almost constant value by means of introducing thicker polymeric spacer and therefore we proved that screening process was successful **(Figure 19b)**.

3.1.3 Surface Morphology

To investigate surface morphology, scanning electron microscopy (SEM) images were observed **(Figure 20a-d)**. It was not fully covered in initial layer. As the layers were stacked, however, the layers were almost fully covered. Furthermore, contrast difference of individual MoS_2 sheets indicated the level of layers was different. To verify that polyelectrolyte is successfully sandwiched by monolayer MoS_2 sheets, transmission electron microscopy (TEM) was used to observe cross-section structure of multilayer sheets **(Figure 20e)**. It showed that uniform layer is developed with polymeric nano-spacing. The thickness of polyelectrolyte was 2.2 nm while that of MoS_2 was 0.69 nm **(Figure 20f)**. The thickness data was accord with that from the ellipsometry displaying average thickness of 2.58 nm for MoS_2/polymer layer **(Figure 21)**.

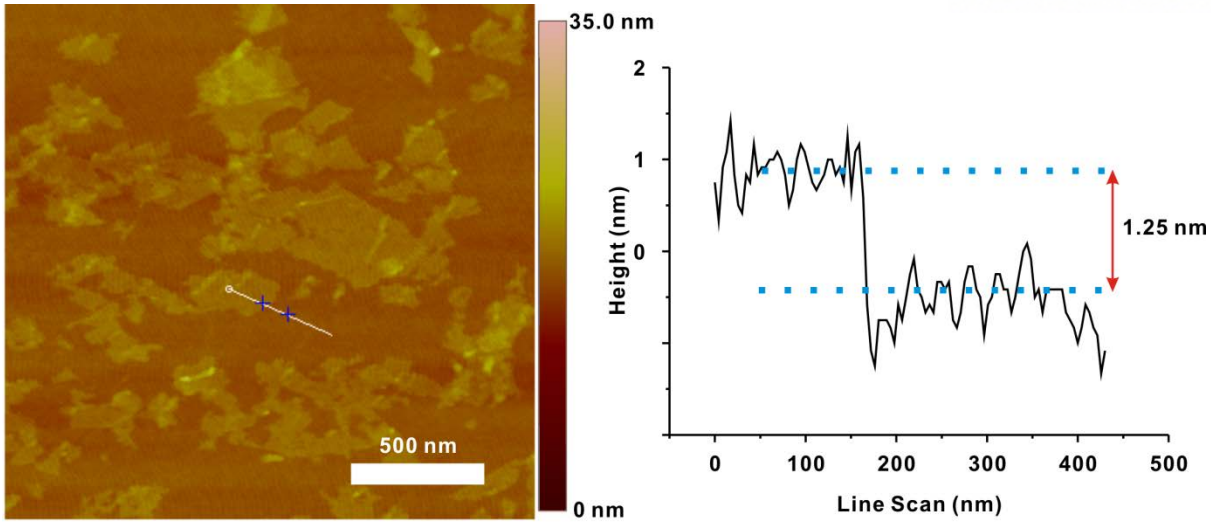

Figure 18. AFM image of MoS2 monolayer exfoliated by Li-intercalation and corresponding line scan profile.

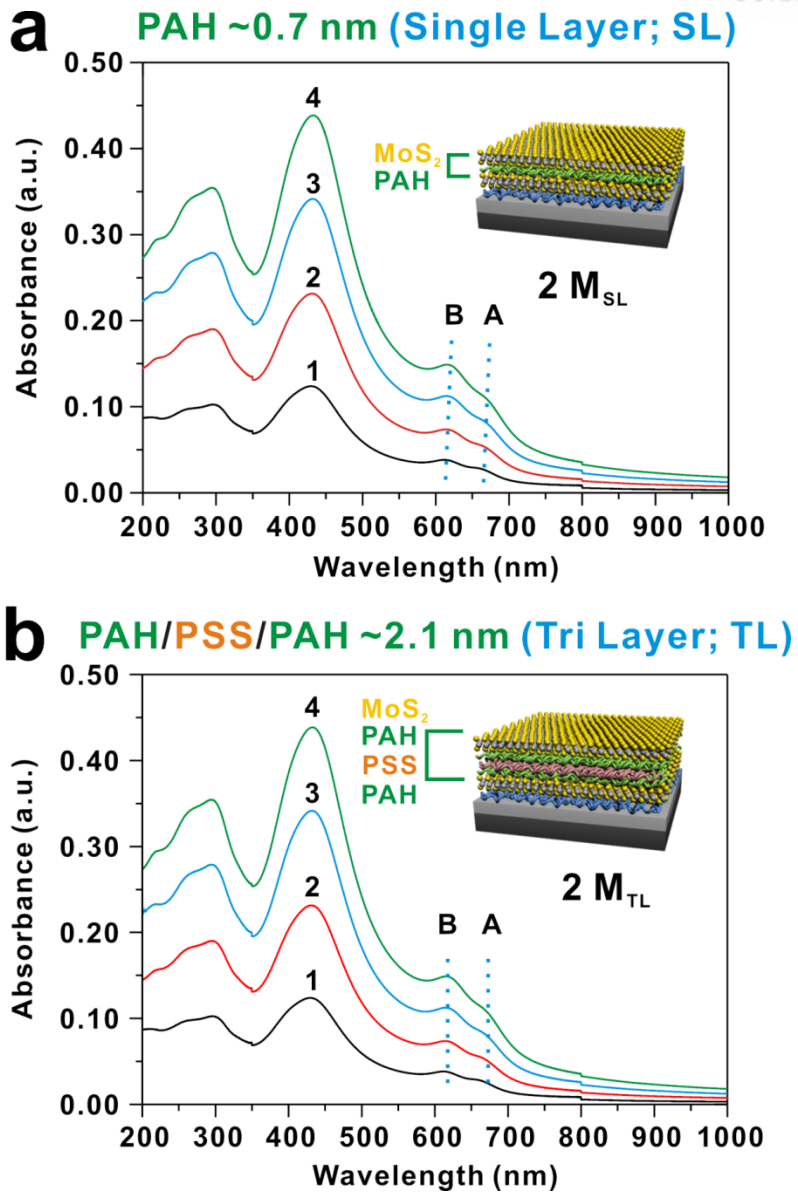

Figure 19. Absorbance spectrum of (a) *n* M_{SL} and (b) *n* M_{TL} set. (*n* = the number of MoS_2 layers) Dotted line indicates excitonic peaks of each sample. Inset is schematic representation of MoS_2 multilayers nanospaced by polymeric single-layer and tri-layer.

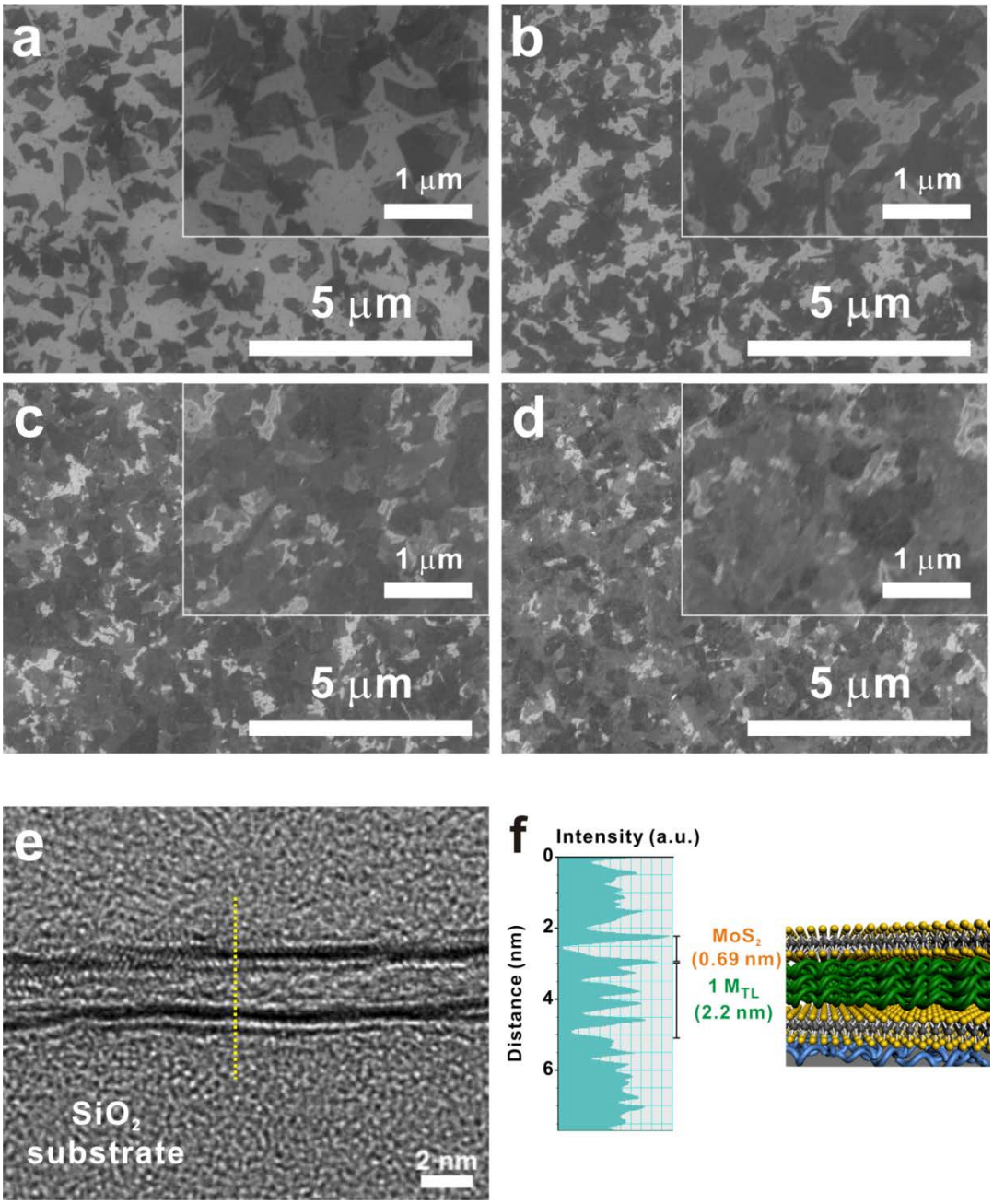

Figure 20. (a) – (d) SEM images of 1 – 4 M_{TL}, respectively. The variation of contrast of each set exhibits level of layer is different. (e) Cross-section TEM image of $2M_{TL}$ and (f) corresponding line scan profile displaying the thickness of monolayer MoS_2 and polymeric tri-layer.

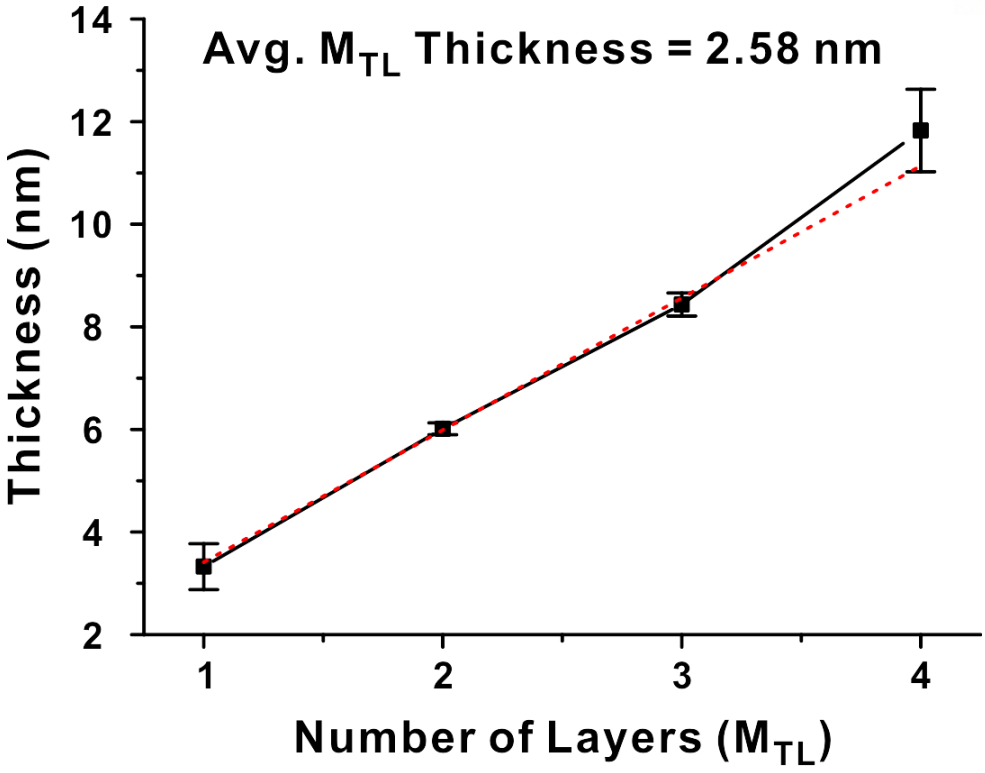

Figure 21. Ellipsometry measurement of *n* M_{TL} set.

3.2 Photoluminescence Analysis - Origin

3.2.1 Photoluminescence and Screening of Interlayer Coupling

To evaluate PL phenomenon and elucidate the origin, the Raman spectrums of 1 - 4 M_{TL} set were observed **(Figure 22a,b)**. Firstly, the Raman vibrational modes of MoS_2 were measured to confirm successful exfoliation. MoS_2 has two characteristic vibrational modes; out-of-plane mode A_{1g} and in-plane mode E^1_{2g}. Previous reports displayed that A_{1g} and E^1_{2g} Raman vibrational modes make shift as the number of layers varied.[66] To be specific, the peak difference between the peaks becomes smaller as MoS_2 layers become thinner due to elimination of interlayer coupling and it reaches ~19 cm^{-1} in monolayer. On the other hand, M_{TL} set showed nearly constant peak separation values regardless of number of layers **(Figure 22c)**. It is strong evidence that polymeric layers successfully isolate MoS_2 sheets and screen interlayer coupling between them. In that reason, PL spectrum demonstrates gradual increase as the number of layers increased **(Figure 22d, e)**.[66,67] To be specific, M_{TL} set exhibits higher photoluminescence behavior than that of M_{SL} set **(Inset of figure 22d)**. This result proves that polymeric tri-layer isolates each MoS_2 layer more effectively.

3.2.2 Polyelectrolyte *p*-doping Effect

Meanwhile, the actual values of peak separation of two vibrational modes are ~21 cm^{-1}, which is slightly larger than that of monolayer. This phenomenon can be explained by doping effect of polymeric layer. There is ~3 cm^{-1} up-shift of A_{1g} mode while E^1_{2g} shows negligible shift **(Figure 22c)**. According to previous work, A_{1g} is very sensitive to carrier concentration while E^1_{2g} mode is almost independent to it.[40,68] The carrier concentration dependency of A_{1g} is based on electron-phonon interaction. MoS_2 conduction band is composed of d_{z^2} orbital which is distributed along *z*-direction.[69] Meanwhile, A_{1g} is out-of-plane mode, that is, *z*-directional vibration. If excess carriers from doping agent are provided, electrons on *d*-orbital interact with *z*-directional vibration. Therefore A_{1g} mode is shifted by electron-phonon interaction. *n*-type doping agent induces down-shift while *p*-type dopant generates up-shift.[40] Based on these results, it can be considered that MoS_2 layers are *p*-doped by polymeric layers. It was found that *p*-doping effect also contributes on PL. If there is no additional effect, it should record 4 times enhancement when PL intensity of 1 and 4 M_{TL} are compared. However, in reality, PL intensity increased by 480% due to contribution of *p*-doping effect **(Figure 22d)**. On the other hand, comparison of PL intensity of 1 and 4 M_{SL} set displayed 347% increased due to imperfect interlayer coupling **(Figure 23)**. For this comparison, PL peak intensity is compared, not areal PL intensity, to consider only optical transition without defect-assisted PL broadening.

The actual charge transfer occurs after annealing process. PAH group has some portion of positively charged amine group. Hydrogen ion can withdraw electron from MoS_2 during the annealing. X-ray photoelectron spectroscopy (XPS) data confirms this speculation. In SL, annealed PAH group displayed significant decrease in portion of NH_3^+ while it was dominant in PAH before annealing **(Figure 24a, b)**.[70] It was accord with the result that Mo composition revealed some defect sites, corresponding to various Mo and S states **(Figure 24c, d)**.[71] Actually, composition of PAH group of TL showed small amount change due to rigid coulomb interaction between PAH and PSS. Since 2 times larger quantity of PAH existed in TL than SL, however, it was sufficient for doping effect.

3.2.3 Three-Level System & Electron Density

To prove whether actual doping effect exists, two kinds of excitonic quasi-particles, exciton and trion, were considered. Trion is charged exciton which is even stable at room temperature on 2D semiconductor while it is unstable in quantum well or 3D structures.[16,20] For simple modelling, it was assumed that there is no positive trion and therefore only negative trion is considered. It is adequate assumption because MoS_2 is unintentionally *n*-type semiconductor. Furthermore, it was also assumed that binding energy is fixed to 30 meV.[20] In reality, binding energy of excitonic quasi-particles can vary because dielectric environment of MoS_2 is changed.[48] To minimize these variations, we designed the structures that MoS_2 is only adjacent to same polyelectrolyte, PAH. Furthermore, three-level system, which is composed of exciton, trion and ground states, is refered from previous reports **(Figure 25)**.[38] In this system, steady state equilibrium is assumed for simplicity. At the three-level system of A^o and A^-, dynamics of the particles are related to their number of particles as described following,

$$\frac{dN_{A^o}}{dt} = G - \{\Gamma_{A^o} + k_{A^-}\}N_{A^o}$$

$$\frac{dN_{A^-}}{dt} = k_{A^-}N_{A^o} - \Gamma_{A^-}N_{A^-}$$

Where G is optical generation rate of exciton and Γ_{A^o}(=0.002 ps^{-1}), Γ_{A^-} (=0.02 ps^{-1}) and k_{A^-} (=0.5 ps^{-1}) are recombination rate of A^o, A^- and formation rate of A^-, respectively. The values are referred from previous reports.[72]

At steady state, the number of particles is

$$N_{A^o} = \frac{G}{\Gamma_{A^o} + k_{A^-}} \cong \frac{G}{k_{A^-}}$$

$$N_{A^-} = \frac{k_{A^-}}{\Gamma_{A^-}}\frac{G}{\Gamma_{A^o} + k_{A^-}} \cong \frac{G}{\Gamma_{A^-}} \ (\because \Gamma_{A^o} \ll k_{A^-})$$

Corresponding photoluminescence intensity is extracted by multiplying radiation rate γ and collection efficiency of photoluminescence.

$$I_{A^o} = \frac{AG\gamma_{A^o}}{k_{A^-}} = AN_{A^o}\gamma_{A^o}$$

$$I_{A^-} = \frac{AG\gamma_{A^-}}{\Gamma_{A^-}} = AN_{A^-}\gamma_{A^-}$$

Under these assumptions and modelling, PL spectrum of every sample were deconvoluted with the PL from exciton (~1.88 eV) and trion (~1.85 eV) **(Figure 26a, b)**. All fitting were conducted with Lorentzian distribution function **(Figure 26c, d)**. From the relation between PL intensity and number of quasi-particle, ratio between PL intensity can be related to the ratio of the number of them. In this process, areal PL intensity was taken into account to consider all electrons under transition. After that, mass action law was applied.[16] Since steady state is assumed by uniform and continuous light illumination, mass action law is valid. Then number of electron is related to the number of A^o and A^- as following,

$$\frac{N_{A^o}n_{el}}{N_{A^-}} = (\frac{m_{A^o}m_e}{\pi^3 h^2 m_{A^-}})k_B T exp(-\frac{E_T}{k_B T})$$

Where E_T is trion binding energy of trion and m_e $(0.35m_o)$, m_{A^o} $(0.8m_o)$ and m_{A^-} $(1.15m_o)$ are effective mass of electron, A^o and A^-, respectively when m_o is free electron mass.

According to previous report, electron density can be extracted by using photoluminescence intensity of exciton and trion.[38]

$$\frac{I_{A^-}}{I_{total}} = \frac{\frac{\gamma_{A^-}}{\gamma_{A^o}}\frac{N_{A^-}}{N_{A^o}}}{1+\frac{\gamma_{A^-}}{\gamma_{A^o}}\frac{N_{A^-}}{N_{A^o}}} \approx \frac{4*10^{-14}n_{el}}{1+4*10^{-14}n_{el}}$$

By this process, actual electron density can be extracted **(Figure 26e)**. Electron density of each sample indicates that actual *p*-doping process exists. For M_{TL} set, doping rate was largely maintained, which resulted in constant electron density of ~5 x 10^{12} cm^{-2} after first decrease in the value. The consistency was accord with effective screening of interlayer coupling between MoS_2 layers. However, M_{SL} set exhibited lower *p*-doping rate but continuous dependency in doping effect which resulted in gradual electron density degradation. This result is fairly consistent with A excitonic PL peak position shift **(Figure 26f)**. We extrapolated that non-adjacent layers also influence the doping level of

individual MoS_2. Moreover, M_{TL} set also shows constant peak position which also indicates eliminated interlayer coupling.

3.2.4 Interparticle Distance Parameter – Criterion for 2D Electronics

2D electronic system reveals exotic physical features and therefore the criterion is necessary to verify that the structure is 2-dimensional. Average interparticle distance (r_s) is demonstrated to elucidate the PL phenomenon in multilayered MoS_2. The r_s value in the unit of effective Bohr radius can be understood by ratio between coulomb potential energy and kinetic energy as following.[20,73]

$$r_s = \frac{g_v}{\sqrt{\pi n}(\frac{\epsilon \hbar^2}{m_e e^2})}$$

where ϵ is the dielectric constant ($\epsilon = \sqrt{\epsilon_{\parallel}\epsilon_{\perp}};\ \epsilon_{\parallel} = 2.5, \epsilon_{\perp} = 6.76$), m_e is the effective mass of an electron ($m_e = 0.35m_o$), g_v is the valley degeneracy ($g_v = 2$) and n is the electron density.[20] In MoS_2 monolayer, the value is ~60 which is much larger value than that of Si-MOSFET, GaAs or SiGe quantum well structures even in low doping level.[73] It was demonstrated that the value became close to 60 as the layers are stacked **(Figure 27)**.

3.3 Performance and Potential Applications

3.3.1 Comparison with MoS_2 from Mechanical Cleavage Method

Solution process accompanies defect sites generated by severe chemical reaction, in this case Li-intercalation. The defects can be scattering sites which drastically degrade PL intensity. Therefore, comparison of physical quantity with MoS_2 from other processes should be provided. Firstly, the quantum yield (QY) value was compared **(Figure 28a)**. The value was comparable in that MoS_2 from mechanical cleavage records ~4.0 x 10^{-3} while MoS_2 multilayers maintained ~1.2 x 10^{-3}.[12] As **figure 28a** displays, QY of M_{TL} set records constant value. Since absorbance rate is gradually increased along the number of layers, corresponding PL intensity also gradually increase. However, QY of M_{SL} set exhibited degradation as they were stacked which was consistent to previous results.[17] In addition, full-width-at-half-maximum (fwhm) value was also investigated because defect mainly assists PL peak broadening **(Figure 28b)**. However, there was no significant difference between mechanically exfoliated MoS_2 and solution based multilayers.[39] Therefore, solution based MoS_2 multilayers are compatible in terms of performance.

3.3.2 Large-Area Application

LbL assembly is versatile tool that provides facile way to synthesize nano-thick film with uniform coverage. Large uniformity of PL intensity was displayed in **figure 29a**. With 400 μm^2, PL intensity showed gradual increase with the number of layers. Since driving force is coulomb interaction, various kinds of charged colloidal suspension are applicable to form vertically stacked rigid and uniform film. Using different combinations of TMDs, hetero multilayers with several bandgaps can be fabricated **(Figure 29b)**. It is expected that such versatility will be essential nutrient for future application of 2D materials.

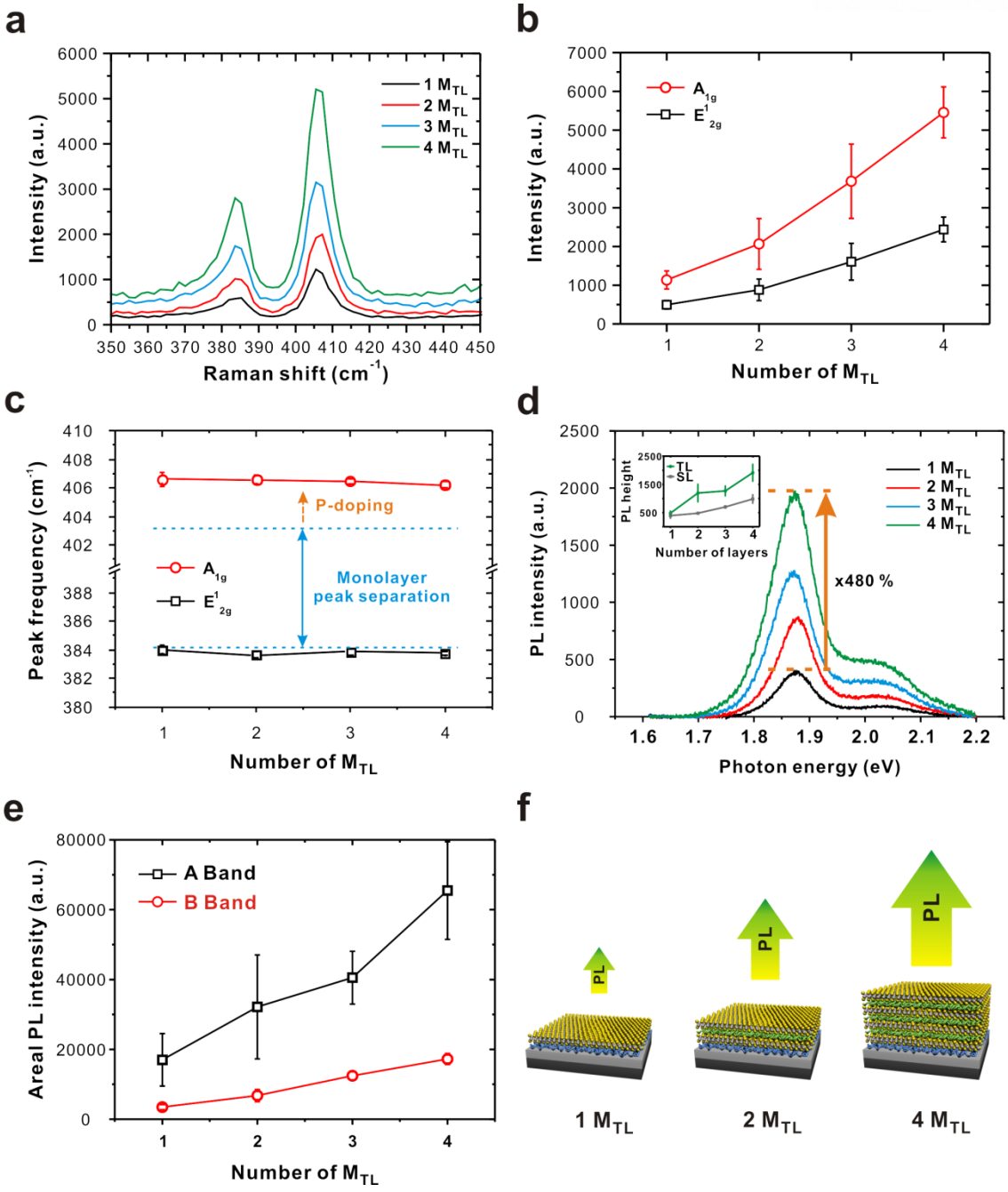

Figure 22. (a) The Raman spectrum of vibrational modes of different layers of MoS_2 M_{TL} set and (b) its intensity. It indicates that film is gradually grown. (c) Peak position of each Raman vibrational modes. Blue dotted line exhibits peak difference of monolayer MoS_2. A_{1g} blue-shift results from p-doping process as indicated in red arrow. (d) Corresponding PL intensity of M_{TL} set. Inset is comparison of the PL intensity between M_{TL} and M_{SL} set. (e) The PL intensity of M_{TL} as a function of number of M_{TL}. Areal intensity is chosen to consider all electrons which are involved in luminescence. (f) Schematic representation of M_{TL} set. MoS_2 is described in yellow colored sulfur and grey colored Mo while polymeric chains are indicated by green (PAH/PSS/PAH) and blue color (PEI).

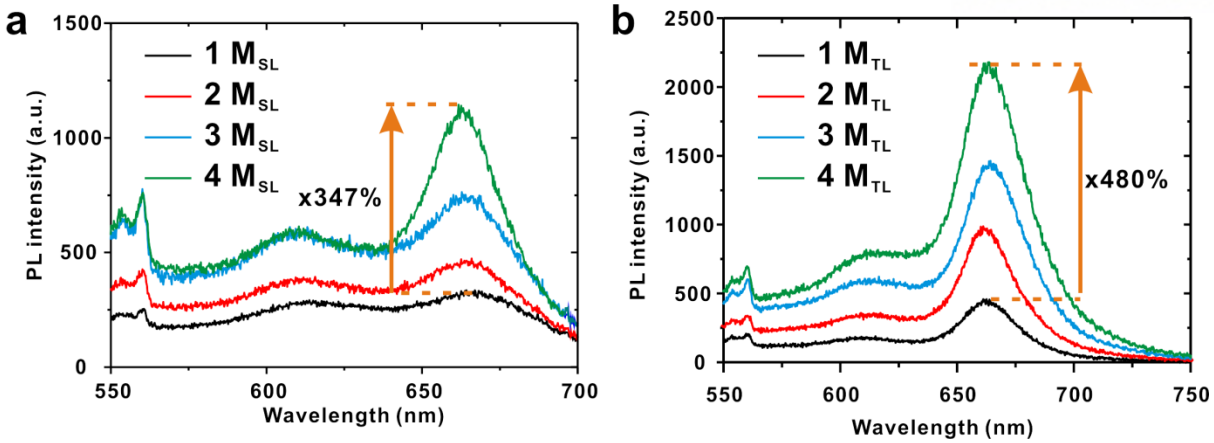

Figure 23. Comparison of PL intensity of (a) M_{SL} and (b) M_{TL} set as a function of wavelength dimension. All the intensities are normalized with Si 1st order peak at 520 cm^{-1}.

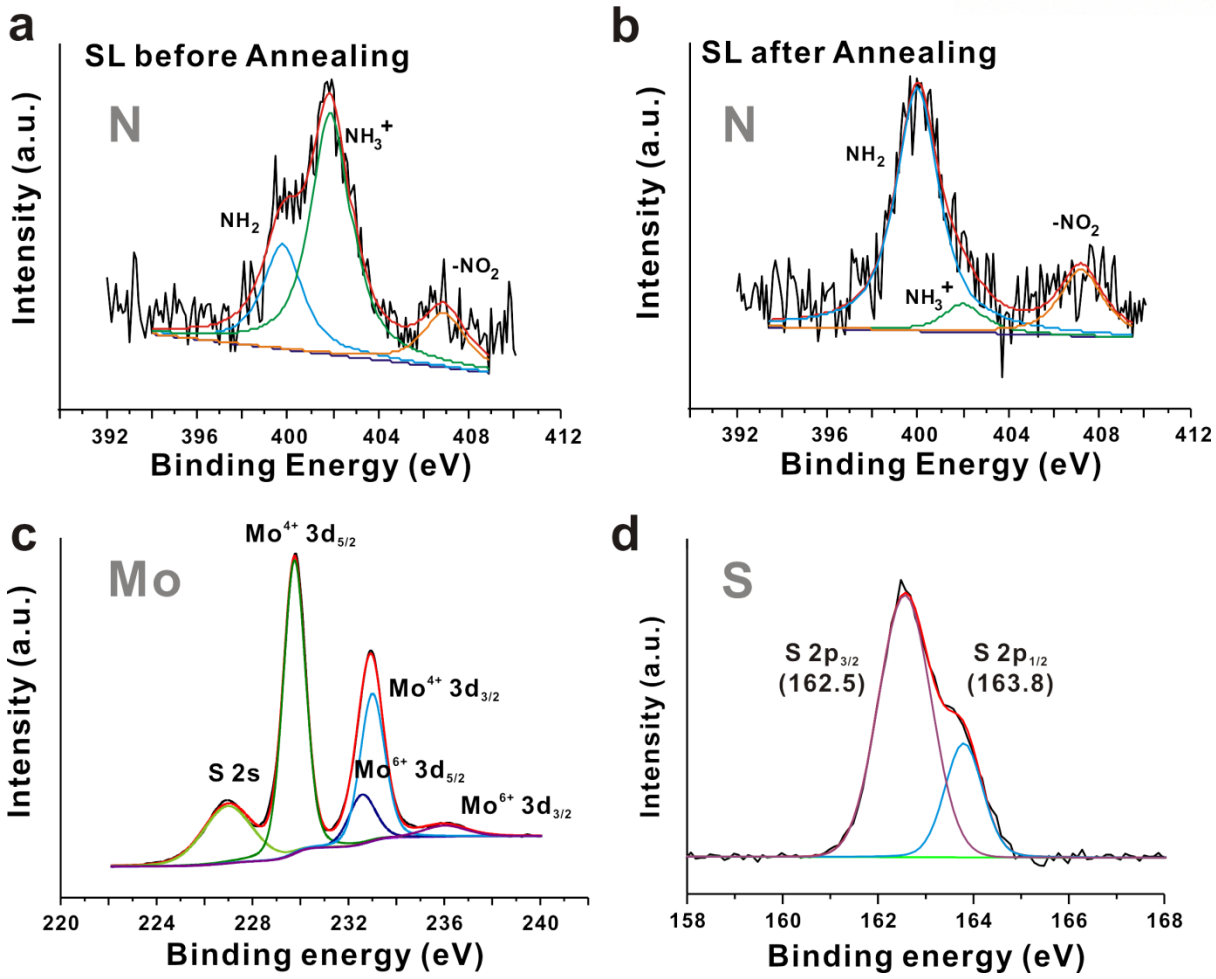

Figure 24. Devonvoluted High- resolution X-ray photoelectron spectroscopy (XPS) spectrum. (a) N 1s spectra of polymeric single layer (PAH) before and (b) after annealing. (c) XPS spectra of Mo 3d and (c) Sulfur 2p of 1 M_{TL} MoS_2 multilayer using previous result. Shirley background is applied to precise fitting.

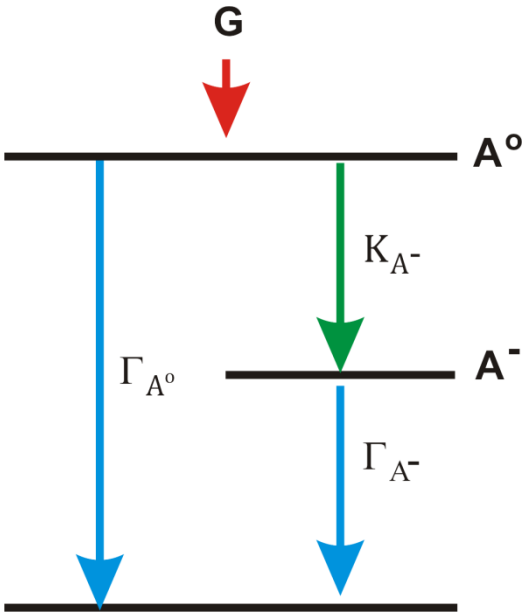

Figure 25. Three-level system of excitonic states. Continuous optical generation (*G*) let the each excitonic quasi-particle (A^o and A^-) be in steady states. Γ_{A^o}, Γ_{A^-} and k_{A^-} are recombination rate of A^o, A^- and formation rate of A^-.

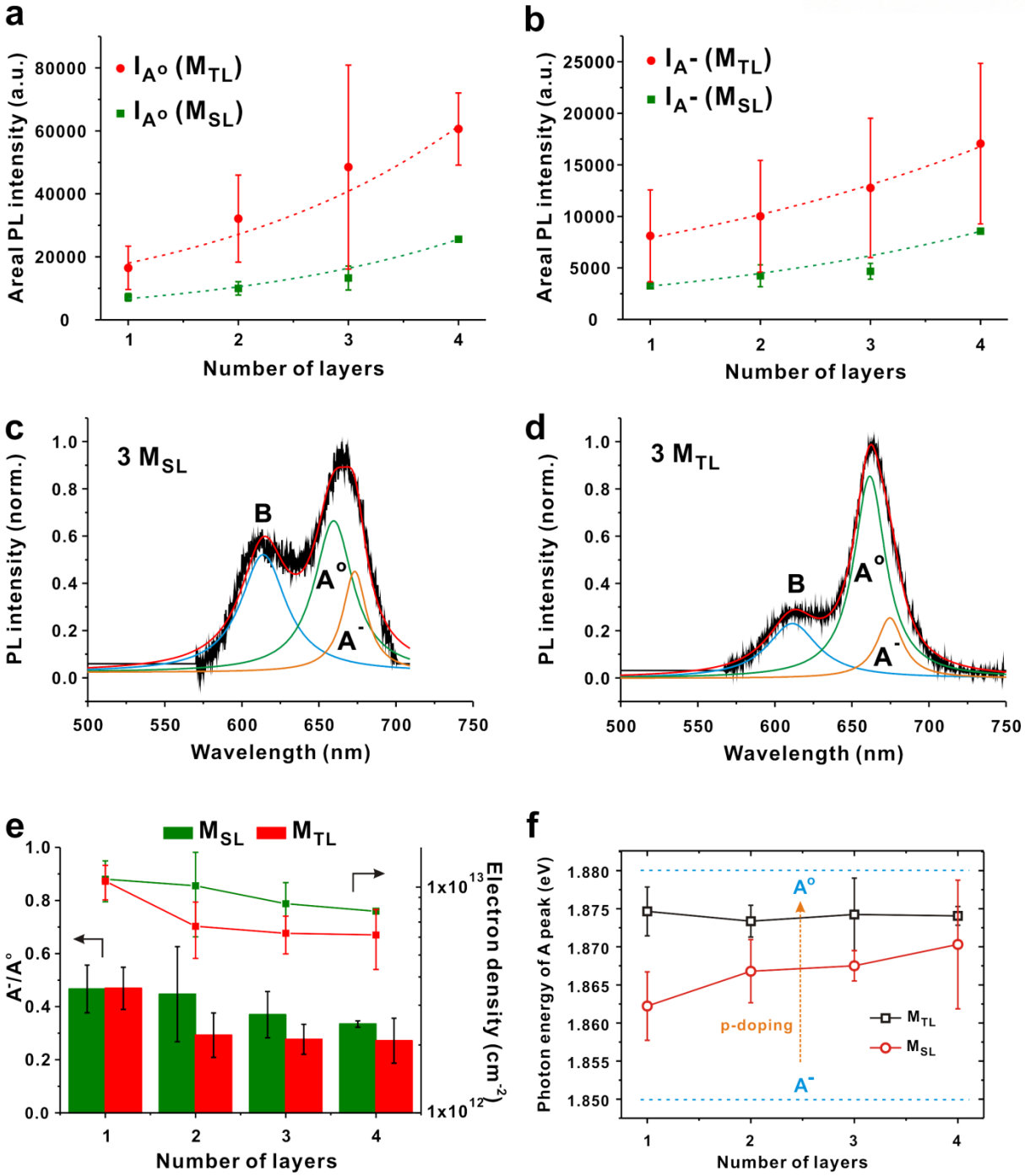

Figure 26. (a, b) Areal PL intensity of MoS_2 multilayers contributed from exciton and trion, respectively. Dotted lines are exponentially fitted line. (c, d) Deconvoluted PL spectrum of the M_{SL} and M_{TL} sets, respectively. (c, d) Ratios of trions and excitons for each layer and the corresponding electron density. (f) Photon energy of A band peaks in M_{TL} and M_{SL} sets.

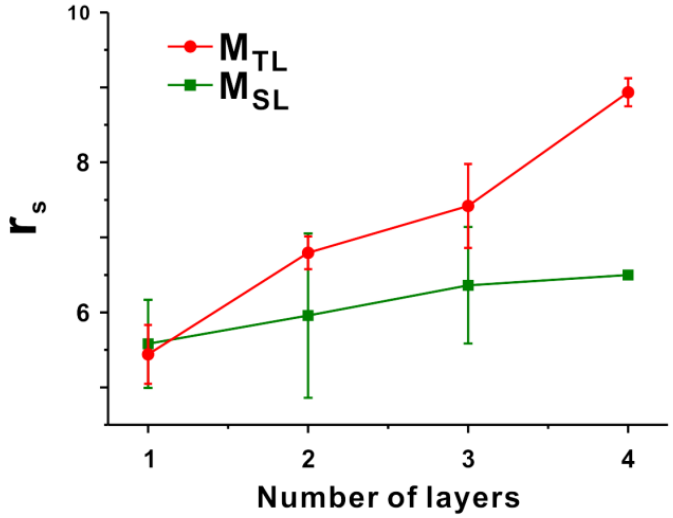

Figure 27. Dimensionless interparticle distance in M_{SL} and M_{TL} set.

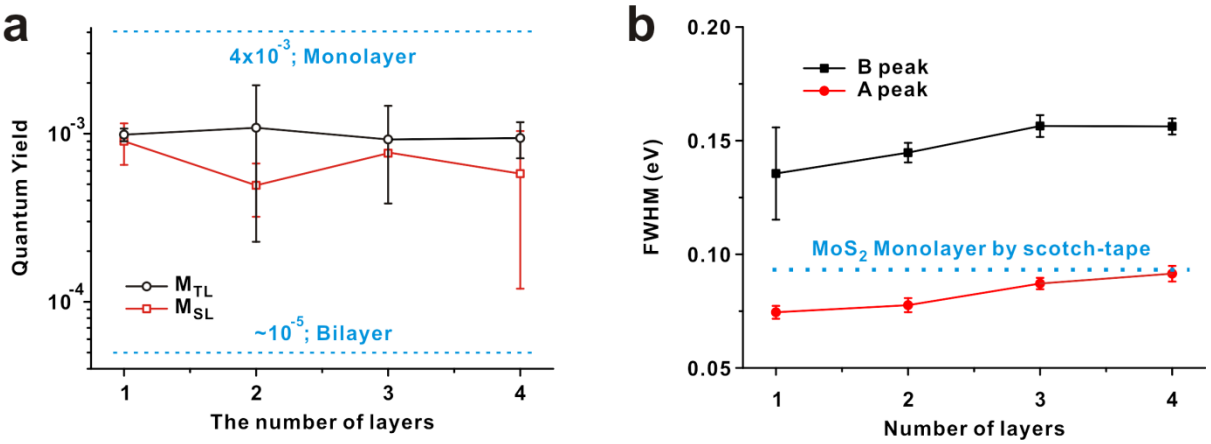

Figure 28. (a) Quantum yield of M_{TL} and M_{SL} sets. (b) full-width-at-half-maximum (fwhm) value of M_{TL} set.

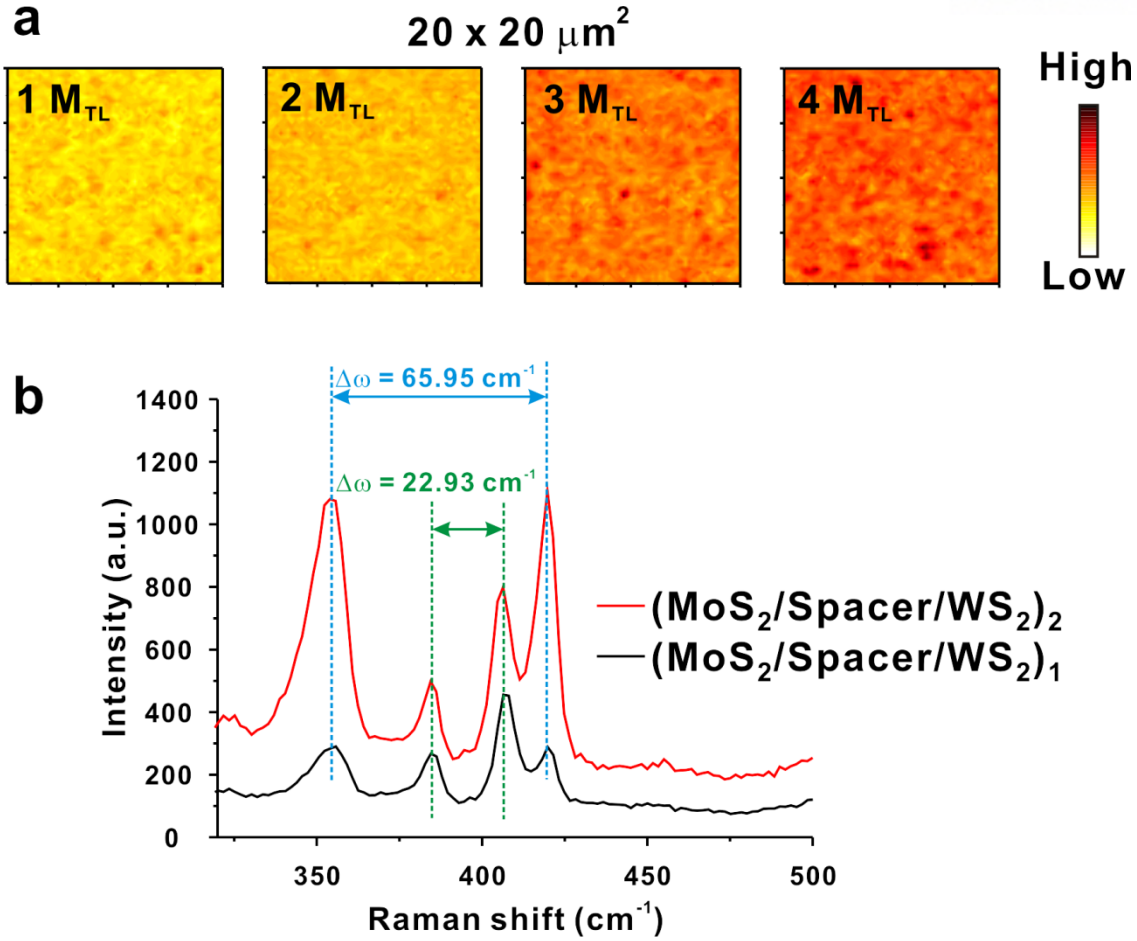

Figure 29. (a) PL intensity mapping of M_{TL} set (20 × 20 μm^2) with a different number of MoS_2 layers. All mappings were conducted with 0.35 mW 532-nm laser for 0.1 s integration time. Signals are obtained from 1.7 to 2.1 eV for each data. (b) Nanospaced MoS_2 and WS_2 heterostructure fabricated by LbL assembly. Green and blue lines are peak difference between E^1_{2g} and A_{1g} of MoS_2 and WS_2, respectively.

IV. Conclusion

As a conclusion, we demonstrate multilayers of MoS_2 with successful isolation of each MoS_2 layers by taking advantage of polymeric spacer **(Figure 30)**. Polyelectrolyte is introduced to successfully screen the interlayer coupling between MoS_2 monolayers. Furthermore, hole is injected to MoS_2 by means of electrolyte behavior of polyelectrolyte. Therefore, both screening of interlayer coupling and doping effect result in enhancement of photoluminescence of MoS_2 multilayers by 480% at maximum compared to that of monolayer MoS_2. By using LbL assembly, it is expected that facile solution-processable vertical structure will extend potential electronic and optoelectronic applications.

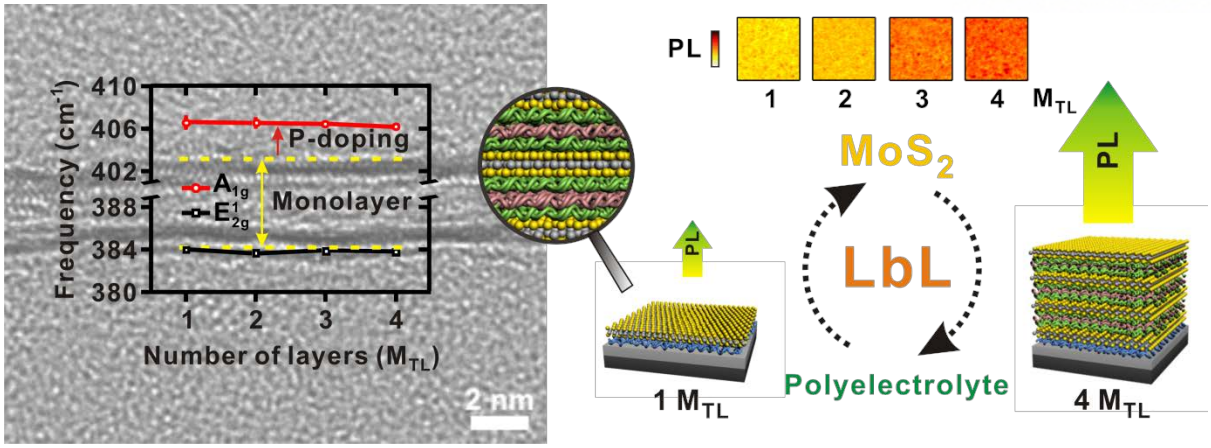

Figure 30. Summary of photoluminescence phenomenon of MoS_2 multilayer.

V. References

1. Geim, A. K.; Novoselov, K. S., The rise of graphene. *Nat. Mater.* **2007,** *6*, 183-191.
2. Novoselov, K. S.; Geim, A. K.; Morozov, S. V.; Jiang, D.; Zhang, Y.; Dubonos, S. V.; Grigorieva, I. V.; Firsov, A. A., Electric Field Effect in Atomically Thin Carbon Films. *Science* **2004,** *306*, 666-669.
3. Novoselov, K., Nobel Lecture: Graphene: Materials in the Flatland. *Rev. Mod. Phys.* **2011,** *83*, 837-849.
4. Novoselov, K. S.; Jiang, D.; Schedin, F.; Booth, T. J.; Khotkevich, V. V.; Morozov, S. V.; Geim, A. K., Two-dimensional atomic crystals. *Proc. Natl. Acad. Sci. U.S.A.* **2005,** *102*, 10451-10453.
5. Li, L.; Yu, Y.; Ye, G. J.; Ge, Q.; Ou, X.; Wu, H.; Feng, D.; Chen, X. H.; Zhang, Y., Black phosphorus field-effect transistors. *Nat Nano* **2014,** *9*, 372-377.
6. Geim, A. K., Graphene: Status and Prospects. *Science* **2009,** *324*, 1530-1534.
7. Zhang, Y.; Tan, Y.-W.; Stormer, H. L.; Kim, P., Experimental observation of the quantum Hall effect and Berry's phase in graphene. *Nature* **2005,** *438*, 201-204.
8. Novoselov, K. S.; Geim, A. K.; Morozov, S. V.; Jiang, D.; Katsnelson, M. I.; Grigorieva, I. V.; Dubonos, S. V.; Firsov, A. A., Two-dimensional gas of massless Dirac fermions in graphene. *Nature* **2005,** *438*, 197-200.
9. Geim, A. K.; Grigorieva, I. V., Van der Waals heterostructures. *Nature* **2013,** *499*, 419-425.
10. Wang, Q. H.; Kalantar-Zadeh, K.; Kis, A.; Coleman, J. N.; Strano, M. S., Electronics and optoelectronics of two-dimensional transition metal dichalcogenides. *Nat. Nanotechnol.* **2012,** *7*, 699-712.
11. Chhowalla, M.; Shin, H. S.; Eda, G.; Li, L. J.; Loh, K. P.; Zhang, H., The chemistry of two-dimensional layered transition metal dichalcogenide nanosheets. *Nature Chem.* **2013,** *5*, 263-275.
12. Mak, K. F.; Lee, C.; Hone, J.; Shan, J.; Heinz, T. F., Atomically Thin MoS_2: A New Direct-Gap Semiconductor. *Phys. Rev. Lett.* **2010,** *105*, 136805.
13. Splendiani, A.; Sun, L.; Zhang, Y.; Li, T.; Kim, J.; Chim, C.-Y.; Galli, G.; Wang, F., Emerging Photoluminescence in Monolayer MoS2. *Nano Lett.* **2010,** *10*, 1271-1275.
14. Xiao, D.; Liu, G.-B.; Feng, W.; Xu, X.; Yao, W., Coupled Spin and Valley Physics in Monolayers of MoS2 and Other Group-VI Dichalcogenides. *Phys. Rev. Lett.* **2012,** *108*, 196802.
15. Kuc, A.; Zibouche, N.; Heine, T., Influence of quantum confinement on the electronic structure of the transition metal sulfide TS2. *Phys. Rev. B* **2011,** *83*, 245213.
16. Ross, J. S.; Wu, S.; Yu, H.; Ghimire, N. J.; Jones, A. M.; Aivazian, G.; Yan, J.; Mandrus, D. G.; Xiao, D.; Yao, W.; Xu, X., Electrical control of neutral and charged excitons in a monolayer semiconductor. *Nat. Commun.* **2013,** *4*, 1474.

17. Eda, G.; Yamaguchi, H.; Voiry, D.; Fujita, T.; Chen, M.; Chhowalla, M., Photoluminescence from chemically exfoliated MoS_2. *Nano Lett.* **2011,** *11*, 5111-5116.

18. King, L. A.; Zhao, W.; Chhowalla, M.; Riley, D. J.; Eda, G., Photoelectrochemical properties of chemically exfoliated MoS2. *J. Mater. Chem. A* **2013,** *1*, 8935-8941.

19. Mak, K. F.; McGill, K. L.; Park, J.; McEuen, P. L., The valley Hall effect in MoS2 transistors. *Science* **2014,** *344*, 1489-1492.

20. Mak, K. F.; He, K.; Lee, C.; Lee, G. H.; Hone, J.; Heinz, T. F.; Shan, J., Tightly bound trions in monolayer MoS_2. *Nat. Mater.* **2013,** *12*, 207-211.

21. Jariwala, D.; Sangwan, V. K.; Lauhon, L. J.; Marks, T. J.; Hersam, M. C., Emerging Device Applications for Semiconducting Two-Dimensional Transition Metal Dichalcogenides. *ACS Nano* **2014,** *8*, 1102-1120.

22. Mak, K. F.; He, K.; Shan, J.; Heinz, T. F., Control of valley polarization in monolayer MoS_2 by optical helicity. *Nat. Nanotechnol.* **2012,** *7*, 494-498.

23. Elliott, R., Intensity of Optical Absorption by Excitons. *Phys. Rev.* **1957,** *108*, 1384-1389.

24. Haug, H.; Koch, S. W. *Quantum Theory of the Optical and Electronic Properties of Semiconductors*. 5th edn, (World Scientific, 2009).

25. Chernikov, A.; Berkelbach, T. C.; Hill, H. M.; Rigosi, A.; Li, Y.; Aslan, O. B.; Reichman, D. R.; Hybertsen, M. S.; Heinz, T. F., Exciton Binding Energy and Nonhydrogenic Rydberg Series in Monolayer WS2. *Phys. Rev. Lett.* **2014,** *113*, 076802.

26. He, K.; Kumar, N.; Zhao, L.; Wang, Z.; Mak, K. F.; Zhao, H.; Shan, J., Tightly Bound Excitons in Monolayer WSe2. *Phys. Rev. Lett.* **2014,** *113*, 026803.

27. Miller, R.; Kleinman, D.; Tsang, W.; Gossard, A., Observation of the excited level of excitons in GaAs quantum wells. *Phys. Rev. B* **1981,** *24*, 1134-1136.

28. Greene, R.; Bajaj, K.; Phelps, D., Energy levels of Wannier excitons in GaAs-Ga1-xAlxAs quantum-well structures. *Phys. Rev. B* **1984,** *29*, 1807-1812.

29. Kheng, K.; Cox, R.; d' Aubigné, M.; Bassani, F.; Saminadayar, K.; Tatarenko, S., Observation of negatively charged excitons X- in semiconductor quantum wells. *Phys. Rev. Lett.* **1993,** *71*, 1752-1755.

30. Huard, V.; Cox, R. T.; Saminadayar, K.; Arnoult, A.; Tatarenko, S., Bound States in Optical Absorption of Semiconductor Quantum Wells Containing a Two-Dimensional Electron Gas. *Phys. Rev. Lett.* **2000,** *84*, 187-190.

31. Scholes, G. D.; Rumbles, G., Excitons in nanoscale systems. *Nat. Mater.* **2006,** *5*, 683-696.

32. Sercombe, D.; Schwarz, S.; Pozo-Zamudio, O. D.; Liu, F.; Robinson, B. J.; Chekhovich, E. A.; Tartakovskii, I. I.; Kolosov, O.; Tartakovskii, A. I., Optical investigation of the natural electron doping in thin MoS2 films deposited on dielectric substrates. *Sci. Rep.* **2013,** *3*, 3489.

33. Zhang, W.; Huang, J.-K.; Chen, C.-H.; Chang, Y.-H.; Cheng, Y.-J.; Li, L.-J., High-Gain

Phototransistors Based on a CVD MoS_2 Monolayer. *Adv. Mater.* **2013,** *25*, 3456-3461.

34. Hui, Y. Y.; Liu, X.; Jie, W.; Chan, N. Y.; Hao, J.; Hsu, Y.-T.; Li, L.-J.; Guo, W.; Lau, S. P., Exceptional Tunability of Band Energy in a Compressively Strained Trilayer MoS_2 Sheet. *ACS Nano* **2013,** *7*, 7126-7131.
35. Li, Z.; Chang, S.-W.; Chen, C.-C.; Cronin, S., Enhanced photocurrent and photoluminescence spectra in MoS2 under ionic liquid gating. *Nano Res.* **2014,** *7*, 973-980.
36. Plechinger, G.; Schrettenbrunner, F. X.; Eroms, J.; Weiss, D.; Schüller, C.; Korn, T., Low-temperature photoluminescence of oxide-covered single-layer MoS2. *Phys. Status Solidi Rapid Res. Lett.* **2012,** *6*, 126-128.
37. Tongay, S.; Suh, J.; Ataca, C.; Fan, W.; Luce, A.; Kang, J. S.; Liu, J.; Ko, C.; Raghunathanan, R.; Zhou, J.; Ogletree, F.; Li, J.; Grossman, J. C.; Wu, J., Defects activated photoluminescence in two-dimensional semiconductors: interplay between bound, charged, and free excitons. *Sci. Rep.* **2013,** *3*, 2657.
38. Mouri, S.; Miyauchi, Y.; Matsuda, K., Tunable Photoluminescence of Monolayer MoS2 via Chemical Doping. *Nano Lett.* **2013,** *13*, 5944-5948.
39. Tongay, S.; Zhou, J.; Ataca, C.; Liu, J.; Kang, J. S.; Matthews, T. S.; You, L.; Li, J.; Grossman, J. C.; Wu, J., Broad-Range Modulation of Light Emission in Two-Dimensional Semiconductors by Molecular Physisorption Gating. *Nano Lett.* **2013,** *13*, 2831-2836.
40. Li, Y.; Xu, C.-Y.; Hu, P.; Zhen, L., Carrier Control of MoS2 Nanoflakes by Functional Self-Assembled Monolayers. *ACS Nano* **2013,** *7*, 7795-7804.
41. Kiriya, D.; Tosun, M.; Zhao, P.; Kang, J. S.; Javey, A., Air-Stable Surface Charge Transfer Doping of MoS2 by Benzyl Viologen. *J. Am. Chem. Soc.* **2014,** *136*, 7853-7856.
42. Choi, M. S.; Qu, D.; Lee, D.; Liu, X.; Watanabe, K.; Taniguchi, T.; Yoo, W. J., Lateral MoS2 p–n Junction Formed by Chemical Doping for Use in High-Performance Optoelectronics. *ACS Nano* **2014,** *8*, 9332-9340.
43. Fang, H.; Chuang, S.; Chang, T. C.; Takei, K.; Takahashi, T.; Javey, A., High-Performance Single Layered WSe2 p-FETs with Chemically Doped Contacts. *Nano Lett.* **2012,** *12*, 3788-3792.
44. Fang, H.; Tosun, M.; Seol, G.; Chang, T. C.; Takei, K.; Guo, J.; Javey, A., Degenerate n-Doping of Few-Layer Transition Metal Dichalcogenides by Potassium. *Nano Lett.* **2013,** *13*, 1991-1995.
45. Gong, Y.; Liu, Z.; Lupini, A. R.; Shi, G.; Lin, J.; Najmaei, S.; Lin, Z.; Elías, A. L.; Berkdemir, A.; You, G.; Terrones, H.; Terrones, M.; Vajtai, R.; Pantelides, S. T.; Pennycook, S. J.; Lou, J.; Zhou, W.; Ajayan, P. M., Band Gap Engineering and Layer-by-Layer Mapping of Selenium-Doped Molybdenum Disulfide. *Nano Lett.* **2013,** *14*, 442-449.
46. Shi, Y.; Huang, J.-K.; Jin, L.; Hsu, Y.-T.; Yu, S. F.; Li, L.-J.; Yang, H. Y., Selective Decoration of Au Nanoparticles on Monolayer MoS2 Single Crystals. *Sci. Rep.* **2013,** *3*, 1839.
47. Prins, F.; Goodman, A. J.; Tisdale, W. A., Reduced Dielectric Screening and Enhanced Energy

Transfer in Single- and Few-Layer MoS2. *Nano Lett.* **2014,** *14*, 6087-6091.

48. Lin, Y.; Ling, X.; Yu, L.; Huang, S.; Hsu, A. L.; Lee, Y.-H.; Kong, J.; Dresselhaus, M. S.; Palacios, T., Dielectric Screening of Excitons and Trions in Single-Layer MoS2. *Nano Lett.* **2014,** *14*, 5569-5576.
49. Coleman, J. N.; Lotya, M.; O'Neill, A.; Bergin, S. D.; King, P. J.; Khan, U.; Young, K.; Gaucher, A.; De, S.; Smith, R. J., Two-dimensional nanosheets produced by liquid exfoliation of layered materials. *Science* **2011,** *331*, 568-571.
50. Joensen, P.; Frindt, R.; Morrison, S. R., Single-layer MoS_2. *Mater. Res. Bull.* **1986,** *21*, 457-461.
51. Lee, Y.-H.; Zhang, X.-Q.; Zhang, W.; Chang, M.-T.; Lin, C.-T.; Chang, K.-D.; Yu, Y.-C.; Wang, J. T.-W.; Chang, C.-S.; Li, L.-J.; Lin, T.-W., Synthesis of Large-Area MoS2 Atomic Layers with Chemical Vapor Deposition. *Adv. Mater.* **2012,** *24*, 2320-2325.
52. Zhan, Y.; Liu, Z.; Najmaei, S.; Ajayan, P. M.; Lou, J., Large-Area Vapor-Phase Growth and Characterization of MoS2 Atomic Layers on a SiO2 Substrate. *Small* **2012,** *8*, 966-971.
53. Liu, K.-K.; Zhang, W.; Lee, Y.-H.; Lin, Y.-C.; Chang, M.-T.; Su, C.-Y.; Chang, C.-S.; Li, H.; Shi, Y.; Zhang, H.; Lai, C.-S.; Li, L.-J., Growth of Large-Area and Highly Crystalline MoS2 Thin Layers on Insulating Substrates. *Nano Lett.* **2012,** *12*, 1538-1544.
54. Radisavljevic, B.; Radenovic, A.; Brivio, J.; Giacometti, V.; Kis, A., Single-layer MoS2 transistors. *Nat. Nanotechnol.* **2011,** *6*, 147-150.
55. Furchi, M. M.; Polyushkin, D. K.; Pospischil, A.; Mueller, T., Mechanisms of Photoconductivity in Atomically Thin MoS2. *Nano Lett.* **2014,** *14*, 6165-6170.
56. Sundaram, R. S.; Engel, M.; Lombardo, A.; Krupke, R.; Ferrari, A. C.; Avouris, P.; Steiner, M., Electroluminescence in Single Layer MoS2. *Nano Lett.* **2013,** *13*, 1416-1421.
57. Yin, Z.; Li, H.; Li, H.; Jiang, L.; Shi, Y.; Sun, Y.; Lu, G.; Zhang, Q.; Chen, X.; Zhang, H., Single-Layer MoS2 Phototransistors. *ACS Nano* **2011,** *6*, 74-80.
58. Lopez-Sanchez, O.; Lembke, D.; Kayci, M.; Radenovic, A.; Kis, A., Ultrasensitive photodetectors based on monolayer MoS2. *Nat. Nanotechnol.* **2013,** *8*, 497-501.
59. Britnell, L.; Ribeiro, R. M.; Eckmann, A.; Jalil, R.; Belle, B. D.; Mishchenko, A.; Kim, Y.-J.; Gorbachev, R. V.; Georgiou, T.; Morozov, S. V.; Grigorenko, A. N.; Geim, A. K.; Casiraghi, C.; Neto, A. H. C.; Novoselov, K. S., Strong Light-Matter Interactions in Heterostructures of Atomically Thin Films. *Science* **2013,** *340*, 1311-1314.
60. Bernardi, M.; Palummo, M.; Grossman, J. C., Extraordinary Sunlight Absorption and One Nanometer Thick Photovoltaics Using Two-Dimensional Monolayer Materials. *Nano Lett.* **2013,** *13*, 3664-3670.
61. Pospischil, A.; Furchi, M. M.; Mueller, T., Solar-energy conversion and light emission in an atomic monolayer p-n diode. *Nat. Nanotechnol.* **2014,** *9*, 257-261.
62. Baugher, B. W. H.; Churchill, H. O. H.; Yang, Y.; Jarillo-Herrero, P., Optoelectronic devices based

on electrically tunable p-n diodes in a monolayer dichalcogenide. *Nat. Nanotechnol.* **2014,** *9*, 262-267.

63. Ross, J. S.; Klement, P.; Jones, A. M.; Ghimire, N. J.; Yan, J.; Mandrus, D. G.; Taniguchi, T.; Watanabe, K.; Kitamura, K.; Yao, W.; Cobden, D. H.; Xu, X., Electrically tunable excitonic light-emitting diodes based on monolayer WSe2 p-n junctions. *Nat. Nanotechnol.* **2014,** *9*, 268-272.
64. Lee, J. E.; Ahn, G.; Shim, J.; Lee, Y. S.; Ryu, S., Optical separation of mechanical strain from charge doping in graphene. *Nat. Commun.* **2012,** *3*, 1024.
65. Yoon, D.; Moon, H.; Son, Y.-W.; Choi, J.; Park, B.; Cha, Y.; Kim, Y.; Cheong, H., Interference effect on Raman spectrum of graphene on SiO2/Si. *Phys. Rev. B* **2009,** *80*, 125422.
66. Lee, C.; Yan, H.; Brus, L. E.; Heinz, T. F.; Hone, J.; Ryu, S., Anomalous lattice vibrations of single-and few-layer MoS_2. *ACS Nano* **2010,** *4*, 2695-2700.
67. Li, S.-L.; Miyazaki, H.; Song, H.; Kuramochi, H.; Nakaharai, S.; Tsukagoshi, K., Quantitative Raman Spectrum and Reliable Thickness Identification for Atomic Layers on Insulating Substrates. *ACS Nano* **2012,** *6*, 7381-7388.
68. Chakraborty, B.; Bera, A.; Muthu, D. V. S.; Bhowmick, S.; Waghmare, U. V.; Sood, A. K., Symmetry-dependent phonon renormalization in monolayer MoS_2 transistor. *Phys. Rev. B* **2012,** *85*, 161403.
69. Fortin, E.; Raga, F., Excitons in molybdenum disulphide. *Phys. Rev. B* **1975,** *11*, 905-912.
70. Lourenço, J. M. C.; Ribeiro, P. A.; Botelho do Rego, A. M.; Braz Fernandes, F. M.; Moutinho, A. M. C.; Raposo, M., Counterions in Poly(allylamine hydrochloride) and Poly(styrene sulfonate) Layer-by-Layer Films. *Langmuir* **2004,** *20*, 8103-8109.
71. Werfel, F.; Minni, E., Photoemission study of the electronic structure of Mo and Mo oxides. *Journal of Physics C: Solid State Physics* **1983,** *16*, 6091.
72. Shi, H.; Yan, R.; Bertolazzi, S.; Brivio, J.; Gao, B.; Kis, A.; Jena, D.; Xing, H. G.; Huang, L., Exciton Dynamics in Suspended Monolayer and Few-Layer MoS2 2D Crystals. *ACS Nano* **2012,** *7*, 1072-1080.
73. Spivak, B.; Kravchenko, S. V.; Kivelson, S. A.; Gao, X. P. A., Colloquium: Transport in strongly correlated two dimensional electron fluids. *Rev. Mod. Phys.* **2010,** *82*, 1743-1766.

VI. Acknowledgement

UNIST에서의 6년은 많은 것을 이루고 더 높은 꿈을 가지게 한 즐거운 도전의 연속이었다고 생각합니다. 1기 입학생으로서 많은 시행착오를 겪었지만 문제에 대한 해답을 찾으려 노력해왔던 과정이 저를 더욱 성장시킬 토대가 될 것이라 확신하며 지금껏 공부에 매진할 수 있는 환경을 제공해준 모교에 깊은 경의를 표합니다.

UNIST에 입학을 결심했던 큰 이유는 학부 때부터 연구경험을 쌓을 수 있을 것이라는 기대감이었습니다. 이러한 의미에서 KBS 연구실에 일찍이 들어갈 수 있었던 것은 큰 행운이라고 생각합니다. 2009년 겨울, 무작정 찾아가 연구실에 들어가고 싶다고 했을 때 흔쾌히 받아주신 김병수 교수님께 진심으로 감사 드립니다. 교수님 연구실에서 보낸 5년이라는 기간이 저의 UNIST 학창시절을 더욱 풍요롭고 가치 있게 만들어 주었다고 생각하며 나아가 더 큰 도약을 위한 기반이 될 것이라 생각합니다.

뿐만 아니라 실험을 배우도록 지도해주신 하버드 대학교 김필립 교수님, 바쁘신 와중에도 학위논문을 심사해주신 박기복 교수님, 김경록 교수님께도 감사의 말씀을 드립니다.

KBS 연구실에서의 경험은 지금의 저를 있게 해준 소중한 시간들이었습니다. 이 기간 동안 함께 했던 연구실 구성원 분들께 감사 드립니다. 다양한 분야에 걸쳐 많은 것들을 알려주신 민사훈 박사님, 정윤경박사님께 감사 드립니다. 또한 항상 먼저 연락해주시고 많은 정보를 제공해주시는 필재형, 든든한 방장이신 은용이 형, 세세한 일들에 대해 묵묵히 도와주셨던 태민이 형과 유리 누나께 감사 드립니다. 아는 정보가 많은 응진이, 진정한 축구인 민수, 현대물리학으로도 몇 차원인지 밝히지 못할 이슬이, 수영하다가도 웃게 만드는 수현이에게 함께 입학한 동기로서 함께해주어 고맙다는 말을 전합니다. 또한 후배지만 배울게 많은 뼛속까지 공학도인 병호, 항상 밝은 웃음으로 맞아주는 민주, 항상 열심히 하며 어른스러운 준희에게 고마움을 전하며 잘 성장하여 연구실의 든든한 기둥이 되기를 희망합니다.

UNIST 학창시절에 있어 5년을 함께한 축구동아리 ‘벡터멘’ 선수들과 매니저들에게 감사의 마음을 전합니다. 특히 축구단 운영에 힘을 써준 1기 부회장 예성이, 훈련부장 준영이, 2기와 3기 회장인 동윤이, 준길이에게 고마움을 전합니다.

항상 힘이 되어주는 좋은 벗들에게도 고마움의 말을 드립니다. UNIST 동기로서 지금은 비록 진로는 달라졌으나 각기 분야에서 열심히 하는 찬울이, 순재, 중환이, 영린이에게 감사의 말을 전합니다. 또한 고등학교 때부터 힘들 때는 어김없이 도움을 주는 훌륭한 친구인 웅희에게도 고맙다는 말을 하고 싶습니다.

기쁨과 슬픔을 공유하며 모이는 날에는 멀리 있어도 어김없이 모이는 허물없는 친구들인 10명의 대한민국 인재상 수상자 친구들에게도 감사합니다. 특히 인격적으로나 실력으로 모두 훌륭하며 고맙게도 항상 먼저 연락해주는 원석이와 본재에게 고마움을 전하고 싶습니다. 또한 더욱 열심히 살아야겠다는 생각을 하게 만드는 UNIST Hu 팸 여러분을 보며 다시금 감사의 인사를 전합니다.

마지막으로 항상 든든한 버팀목이 되어주시며 무한한 사랑으로 저를 보살펴주신 아버지와 어머니 그리고 항상 진실된 마음으로 응원해주는 누나에게 깊은 감사를 드립니다.

도전으로 시작되었던 모교와의 만남이 이제 또 다른 도전으로 이어지려 합니다. 이 새로운 시작을 즐기는 마음으로 받아들이며 이제껏 해오던 것처럼 묵묵히 앞을 향해 걸어가겠습니다.